CHAPTER 3

RESULTS AND DISCUSSION

3.1 Preparation of pure TiO_2 and V, Cu, Fe-doped TiO_2 powders

In the modified sol-gel process, all samples were prepared by the reactions of hydrolysis and condensation of a titanium alkoxide precursor, $Ti(OR)_n$. The process was developed to effectively control the diffusion rates of reactants in hydrolysis and condensation reactions by using cellophane membranes. This process demonstrated good reproducibility for both preparations of pure TiO_2 and V, Cu, Fe-doped TiO_2. Moreover, the use of cellophane membrane pouch eliminated the cumbersome steps such as conventional precipitate filtration, and improved ability to obtain uniform small particle sizes, and facilitated the production of high purity products. Condensation reaction including oxolation and olation, which then transformed into an oxide network. The olation step could leave the alcohol molecule which is coming from a protonated alkoxy ligands and water molecule coming from a solvated alkoxide. The condensation by oxolation of alkoxide could transform to alkoxy ligand and to hydroxo ligand and eventually to form the oxo. The reaction schemes were described by reaction (1.15)-(1.18) in Chapter 1. Particles of titanium hydroxides produced from sol-gel route in aqueous medium generally possesses electrical charge due to the amphoteric dissociation of surface hydroxyl groups and the adsorption of H^+/OH^- . In this modified sol-gel process, the pH of sol in the reaction was slightly increasing and constant value pH 8 though out until the reaction was finished, possibly due to ammonium hydroxide solution diffuse though cellophane membrane barrier in a uniform rate. The cellophane membrane therefore, was used for controlling hydrolysis and condensation reaction as the migrations of H^+ and OH^- ions that subsequently affect the rate of hydrolysis and condensation reaction.

The Fe-doped TiO_2 was prepared by the impregnation method with a high degree of reproducibility. The impregnation method has many advantages such as the actual amount of doping iron on TiO_2 could be prepared and was easy for preparing the doped catalysts. When doping with iron under the same amount of Fe dopant, it could be seen the different color of the powder obtained when prepared by the impregnation method and the modified sol-gel method. The color of Fe-doped TiO_2 prepared by the impregnation method was dark reddish color, while Fe-doped TiO_2 prepared by the modified sol-gel method was less reddish at the same amount of iron.

3.2 Samples characterization

3.2.1 UV-Vis diffuse reflectance spectroscopy studies

The absorption spectra of pure TiO_2 and transition metal ions (V, Cu, and Fe) doped TiO_2 were obtained by analyzing the reflectance measurement with Kubelka-Munk emission function, $F(R_\infty)$ given by the equation:

$$F(R_\infty) = \frac{(1-(R_\infty))^2}{2R_\infty} \tag{3.1}$$

$F(R_\infty)$ is proportional to the absorption constant of the material, it is indicative of the absorptivity of the sample at a particular wavelength. The band gap energy were obtained from the plot between $E_g = \frac{1241}{\lambda_{onset}}$ and $[F(R)h\upsilon]^{1/2}$; where E_g is the band gap energy in unit of eV and λ_{onset} in unit of nm.

The baseline correction was performed using a calibrated sample of MgO. The spectra were recorded at room temperature in the range of 300-700 nm. The UV-Vis diffuse reflectance spectra, absorbance Kubelka-Munk and band gap energy of pure TiO_2 and V, Cu, Fe-doped TiO_2 prepared by the modified sol-gel method are shown in Figure 3.1-3.3 and Fe-doped TiO_2 prepared by the impregnation method is shown Figure 3.4.

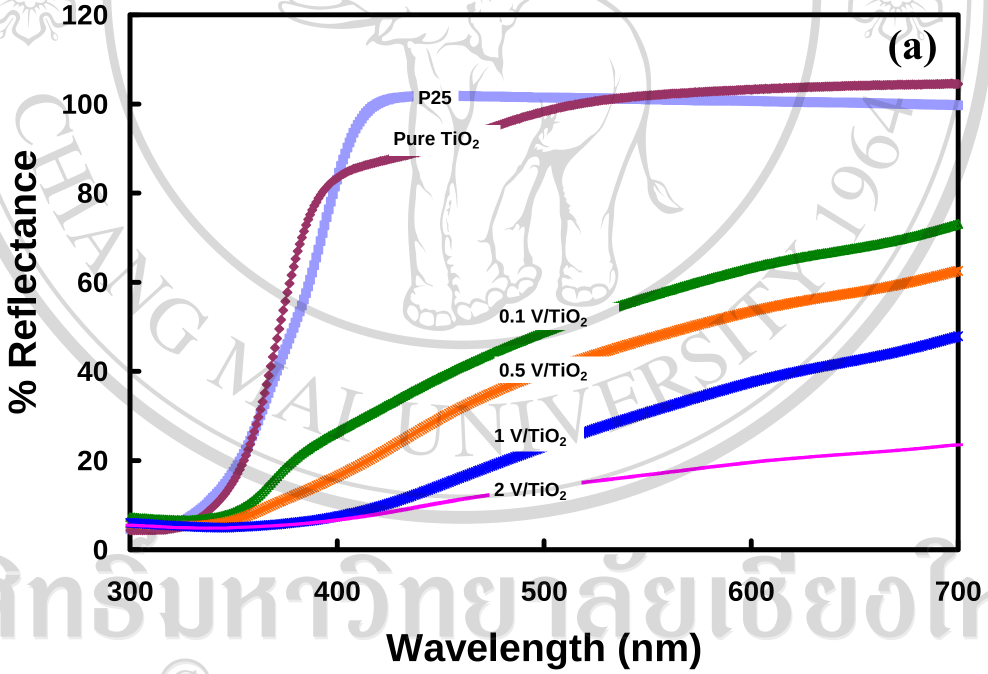

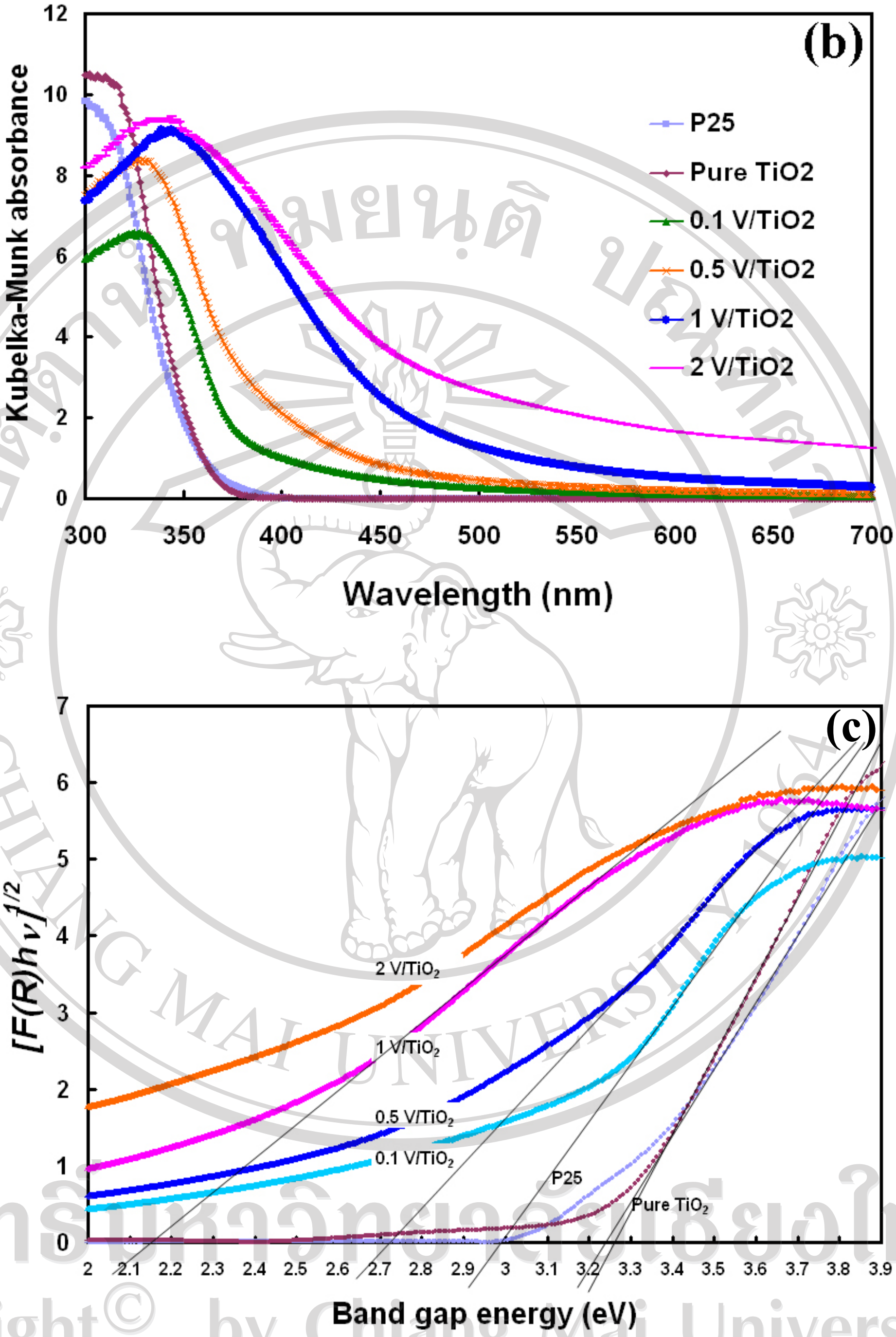

Figure 3.1 UV-Vis (a) reflection spectra, (b) absorbance Kubelka-Munk, and (c) relation between band gap energy and $[F(R)h\upsilon]^{1/2}$ of P25, pure TiO_2 and 0.1-2 at.% of V-doped TiO_2

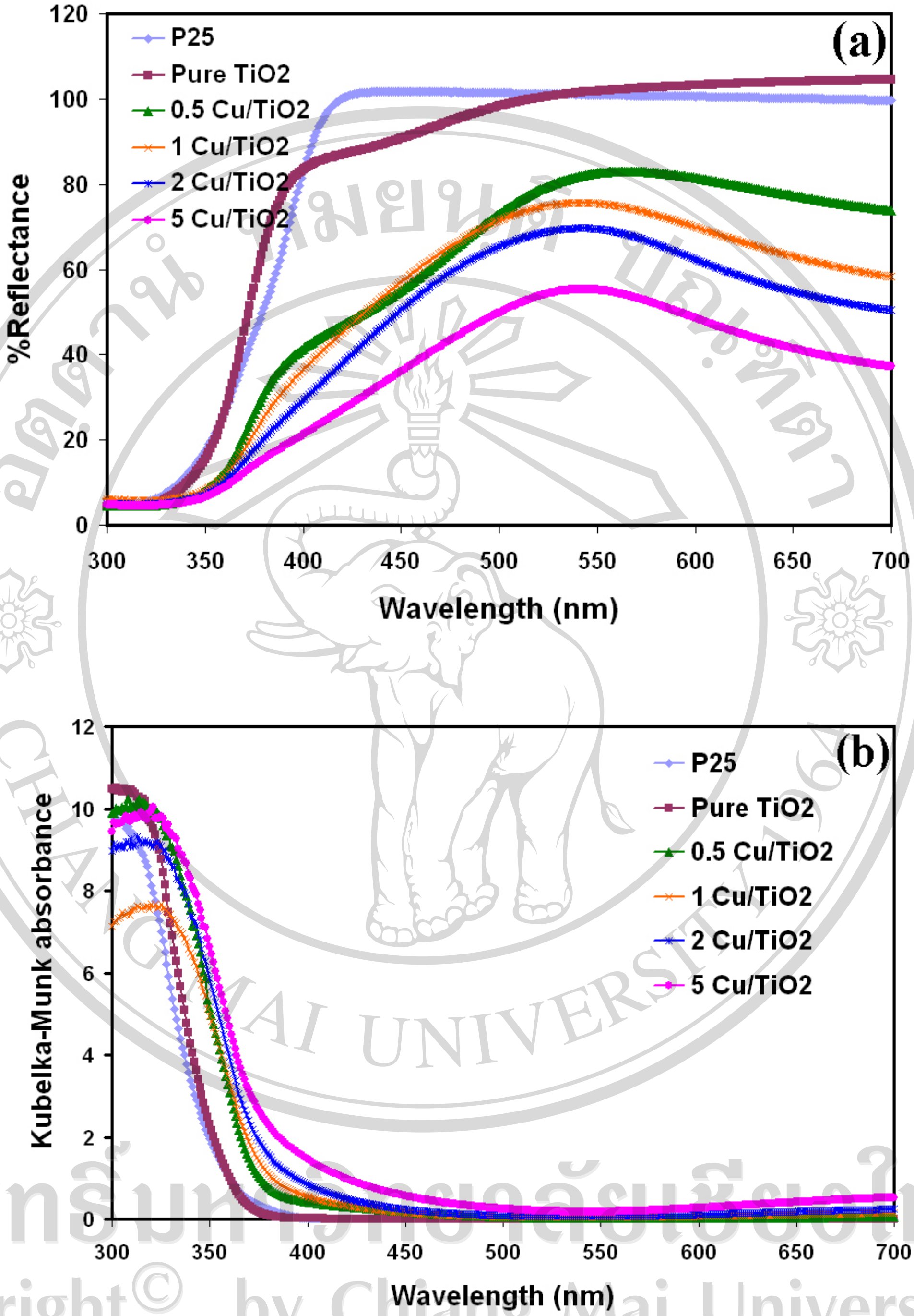
(a)
%Reflectance
120
100
80
60
40
20
0
300
350
400
450
500
550
600
650
700
Wavelength (nm)
P25
Pure TiO2
0.5 Cu/TiO2
1 Cu/TiO2
2 Cu/TiO2
5 Cu/TiO2
(b)
Kubelka-Munk absorbance
12
10
8
6
4
2
0
300
350
400
450
500
550
600
650
700
Wavelength (nm)
P25
Pure TiO2
0.5 Cu/TiO2
1 Cu/TiO2
2 Cu/TiO2
5 Cu/TiO2

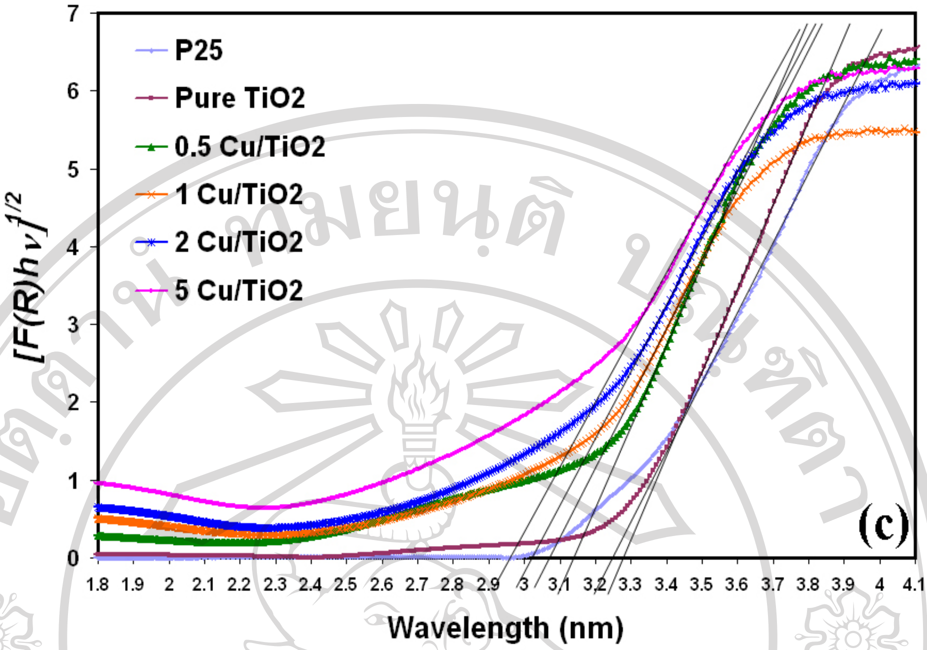

Figure 3.2 UV-Vis (a) reflection spectra, (b) absorbance Kubelka-Munk, and (c) relation between band gap energy and $[F(R)h\upsilon]^{1/2}$ of P25, pure TiO_2 and 0.5-5 at.% of Cu-doped TiO_2

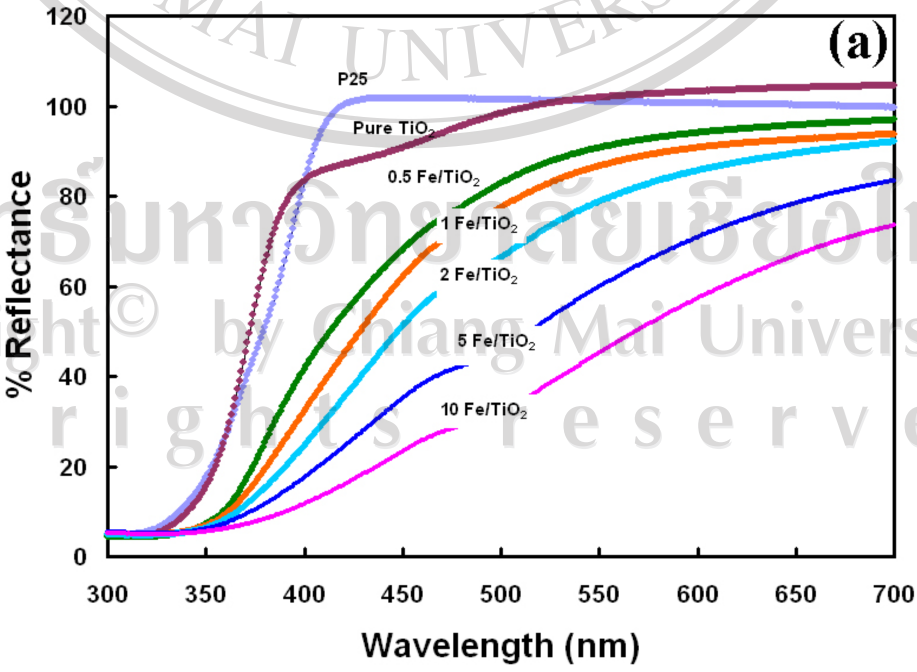

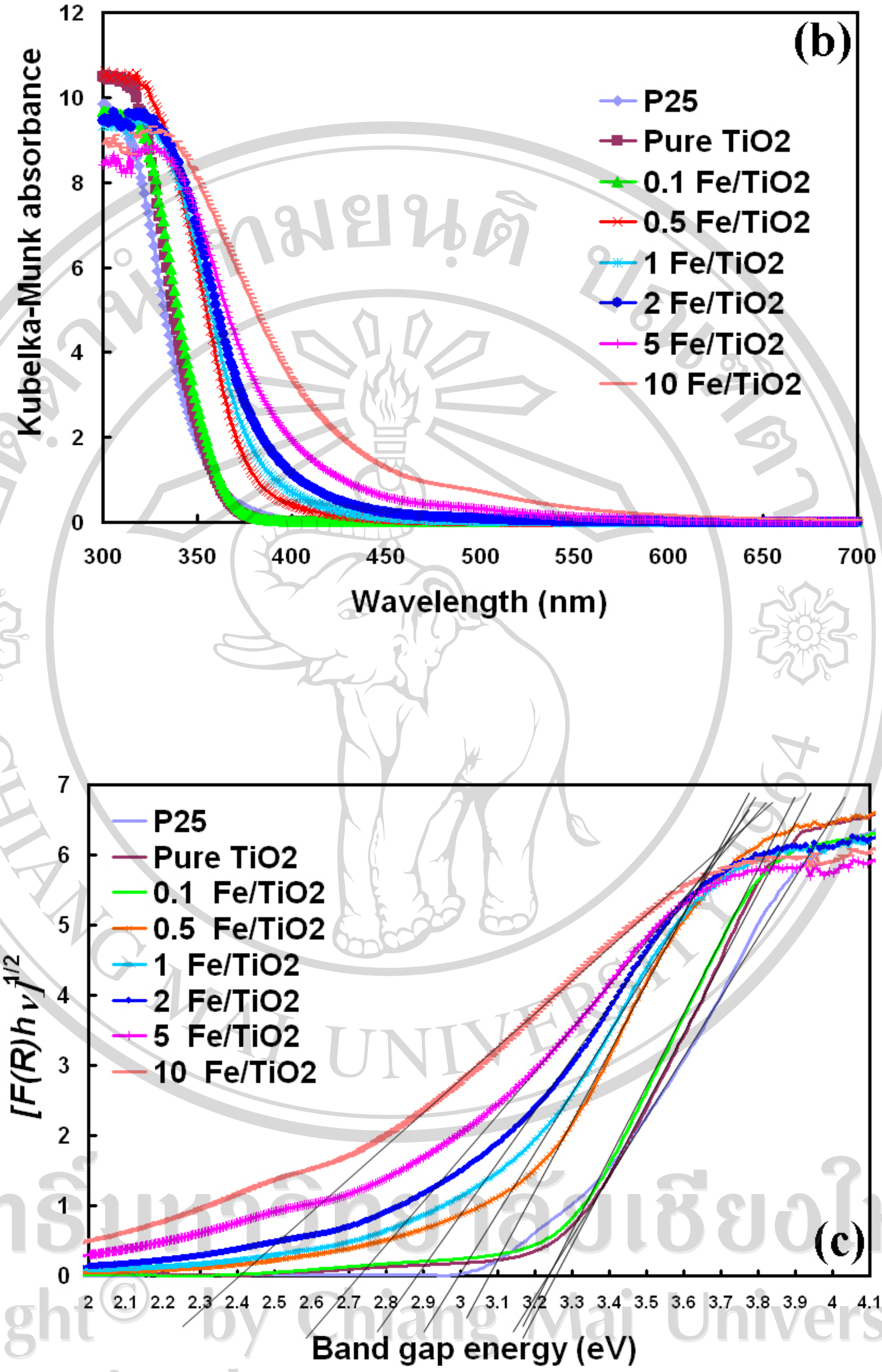

Figure 3.3 UV-Vis (a) reflection spectra, (b) absorbance Kubelka-Munk, and (c) relation between band gap energy and $[F(R)h\upsilon]^{1/2}$ of P25, pure TiO_2 and 0.1-10 at.% of Fe-doped TiO_2 prepared by the modified sol-gel method

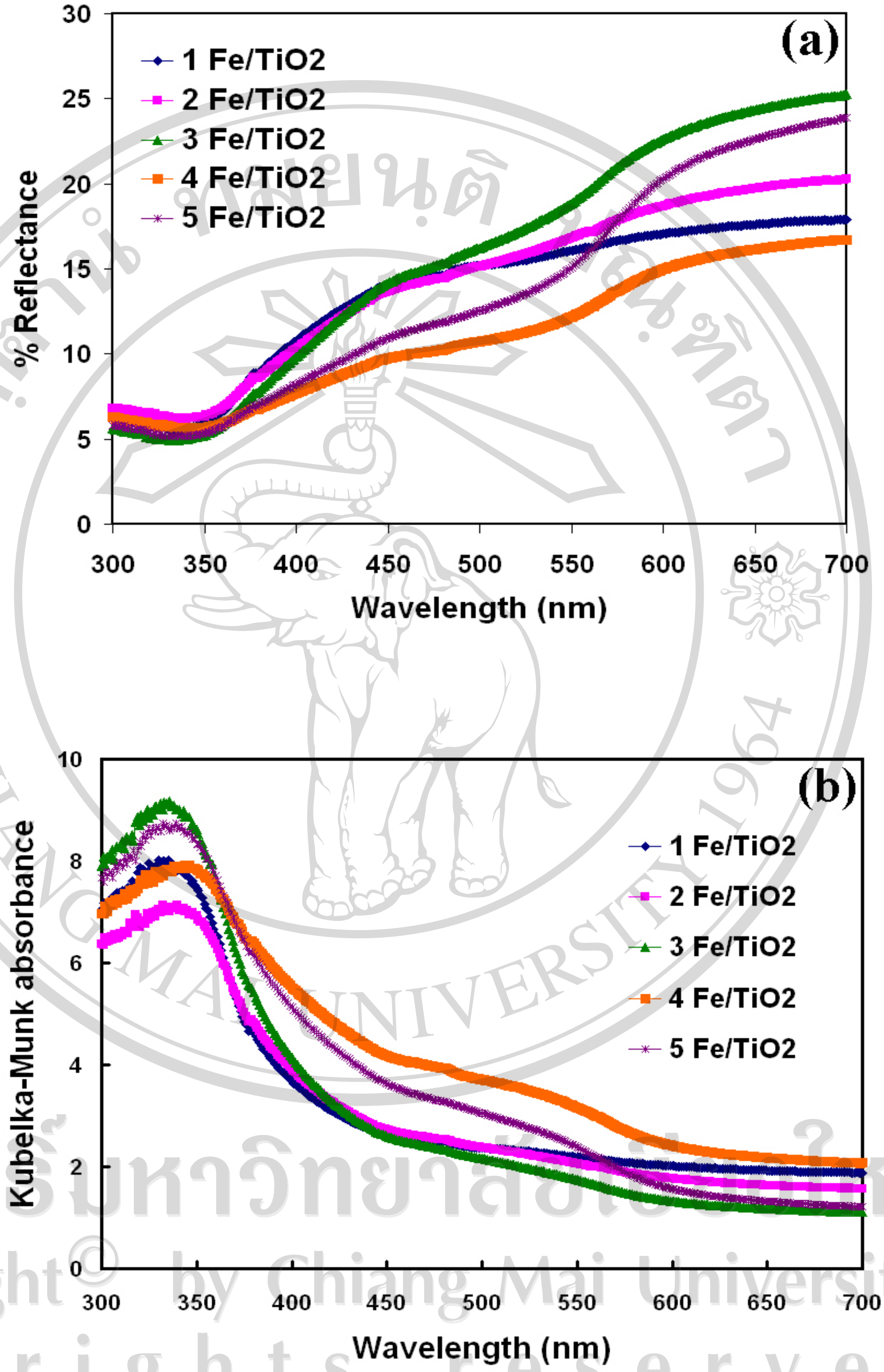
(a)
% Reflectance
30
25
20
15
10
5
0
300
350
400
450
500
550
600
650
700
Wavelength (nm)
1 Fe/TiO2
2 Fe/TiO2
3 Fe/TiO2
4 Fe/TiO2
5 Fe/TiO2
(b)
Kubelka-Munk absorbance
10
8
6
4
2
0
300
350
400
450
500
550
600
650
700
Wavelength (nm)
1 Fe/TiO2
2 Fe/TiO2
3 Fe/TiO2
4 Fe/TiO2
5 Fe/TiO2

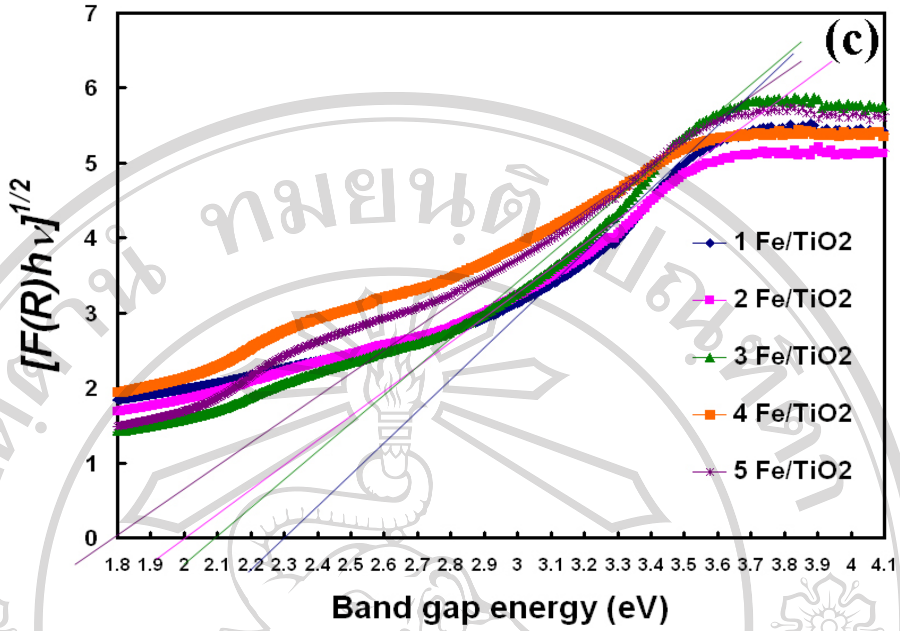

Figure 3.4 UV-Vis (a) reflection spectra, (b) absorbance Kubelka-Munk, and (c) relation between band gap energy and $[F(R)h\upsilon]^{1/2}$ of P25, pure TiO_2 and 1-5 at.% of Fe-doped TiO_2 prepared by the impregnation method

UV-Vis reflectance analysis was carried out from the reflectance spectra of dry-pressed sample measurement then converted to absorbance spectra using Kubelka-Munk function. Figure 3.1(a), 3.2(a), 3.3(a), 3.4(a) showed the onset of reflectance spectra of V, Cu, Fe-doped TiO_2 prepared by the modified sol-gel method in comparison with the impregnation method. Figure 3.1(b), 3.2(b), 3.3(b), 3.4(b) showed the onset of absorption was shifted to longer wavelengths on doping TiO_2 with vanadium, iron, and copper. With an increasing in vanadium, iron, and copper content, the enhanced absorption was observed in the visible region. Therefore, all doping with vanadium, copper, and iron ions can enhance photocatalytic activity under visible region. Figure 3.1(c), 3.2(c), 3.3(c), 3.4(c) showed the relation between band gap energy and $[F(R)h\upsilon]^{1/2}$ in the spectra of V, Cu, Fe-doped TiO_2. The doping with V, Cu, and Fe created in subband resulted in narrowing the band gap. An increased amount of V-doped TiO_2 from 0.1-1 at.%, the absorption threshold of V-doped TiO_2 increased, while the vanadium ion created in subband resulted in narrowing the band gap from 3.0 to 2.16 eV as shown in Figure 3.1(c). Figure 3.2(c) shows the absorption threshold of Cu-doped TiO_2 increased, while the copper ion created in subband resulted in narrowing the band gap from 3.14 to 2.95 eV. The amount of 0.1-10 at.% Fe-doped TiO_2 prepared by the modified sol-gel method, the absorption threshold increased while the iron ion created in subband resulted in narrowing the band gap from 3.22 to 2.41 eV as shown in Figure 3.3(c). An increased amount of 1-5 at.% Fe-doped TiO_2 prepared by the impregnation method, the absorption threshold of Fe-doped TiO_2 increased while the iron ion created in subband resulted in narrowing the band gap from 2.3 to 1.8 eV as shown in Figure 3.4(c). It could be seen that the band gap energy of Fe-doped TiO_2 prepared by the impregnation method was lower than Fe-doped TiO_2 prepared by the modified sol-gel method. Therefore, the narrow band gap energy caused an easiness for excited electron from valence band to conduction band. Moreover, narrow band gap energy enables lower energy for excitation of an electron or to produce of an electron and a hole. Anpo and Takeuchi [99] reported that V, Mn, and Cr ions doped TiO_2 were prepared by metal ion-implantation techniques. UV-Vis absorption spectra showed shifts in adsorption band toward visible light regions.

p-Type doping obtained by dissolving heterocations of valencies was lower than that of Ti^{4+} (Fe^{3+} and Cu^{2+}) in the TiO_2 lattice, while n-type doping was obtained by heterocations of valencies was higher than +4 (Nb^{5+}, Ta^{5+}, Sb^{5+}). In this research

TiO_2 was doped with transition metal p-type cations (V^{4+}, Fe^{3+} and Cu^{2+}). The inhibition effect was ascribed to an increase in the electron–hole recombination rate. More precisely, p-type dopants act as acceptor centers, which trap photoelectrons and once negatively charged to attract holes, thus forming recombination centers. On the other hand, n-type dopants act as donor centers [1].

Doping with V, Cu, and Fe cations into TiO_2 lattice, results in the formation of impurity energy level between the conduction band and valence band of TiO_2. The impurity energy level allows for intrinsic band gap excitation such that under illumination of visible light, the higher energy state of 3d-electrons from cations dopant can be excited to the conduction band of TiO_2. Factors related to the electronic structure seem to be more important, associated with the fact that dopant ions influence charge separation, charge-carrier recombination and interfacial charge-transfer rates. In addition, the recombination rate increased with the dopant concentration because the distance between trapping sites in a particle decreased with the number of dopants. Navío et al. (1996) [97] reported that the diffuse reflectance spectra of samples were not well resolved for indicating a large dispersion and disorder of transition metal ions species in the TiO_2 lattice and surface. The absorptions spectra were increased in visible region could be due to transitions implicating surface states or native defects in the lattice.

3.2.2 BET- Specific surface area studies

BET adsorption of nitrogen gas for surface area determination at the temperature of liquid nitrogen was performed on pure TiO_2 and V, Cu, Fe-doped TiO_2 prepared by the modified sol-gel method. Sample of pure TiO_2 calcined at 400 °C for

3h possessed high specific surface area of 121 m^2/g and the specific surface area decreased appreciably to 17 m^2/g with increasing the calcination temperature up to 600 °C as shown in Figure 3.5. The high calcination temperature correlated with the small specific surface area for the large particle sizes. The surface hydroxyl groups, heat treatment, and surface area were related to the influence on photocatalytic performance. The high heat treatment step was known of leading to the loss of surface hydroxyl groups. The decreasing hydroxylation of surface groups was considered to be the most likely reason for lower photoactivity on rutile phase at high temperature. The higher surface area of anatase was also known to be a contributing factor for its higher activity when compared with rutile.

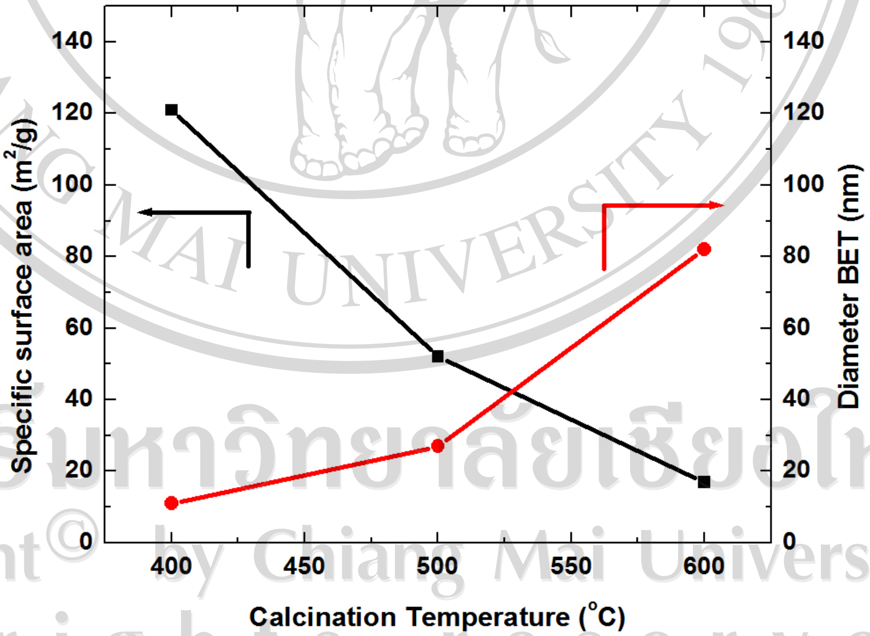

Figure 3.5 SSA and BET equivalent diameter of pure TiO_2 at different calcination temperatures of 400-600 °C for 3h

The BET specific surface area (SSA) results were found that increase amount of V, Cu and Fe doping in TiO_2 enable the increase in specific surface area and possibly increase in photocatalytic activity (Figure 3.6-3.9). However, the higher amount of 2 at.% of V dopant were causing the lower specific surface area as in the case of 5 at.% of Cu doping. Hence, the decrease in specific surface area possibly decreased the photoactivity due to the smaller surface area of catalyst to adsorb the compound on the catalyst surface. The specific surface area of 0.1-2 at.% V-doped TiO_2 decreased from 41-22 m^2/g, corresponding to BET equivalent diameters of 34 to 63 nm, respectively. The specific surface area of 0.5-5 at.% of Cu-doped TiO_2 increased from 73-107 m^2/g, corresponding to BET equivalent diameters of 19 to 11 nm, respectively. BET equivalent diameter of V and Cu-doped TiO_2 decreased with increasing amount of dopant contents and then increased with higher amount of V and Cu dopants as shown in Figure 3.6 and 3.7. The BET equivalent diameter of Fe-doped TiO_2 prepared by the modified sol-gel method decreased with increasing amount of iron dopant until 10 at.% as shown in Figure 3.8. The tendency of specific surface area of Fe-doped TiO_2 prepared by the modified sol-gel method increased with increasing amount of iron but the specific surface area of 0.5 at.% of Fe-doped TiO_2 was higher than 1 at.% of Fe-doped TiO_2 may be due to an error from the experiment as shown in Figure 3.8. The specific surface area of 0.1-10 at.% of Fe-doped TiO_2 increased from 75-156 m^2/g, corresponded to BET equivalent diameters of 20 to 10 nm, respectively. Figure 3.9 showed the specific surface area and BET equivalent diameter of Fe-doped TiO_2 prepared by the impregnation method. The specific surface area of 2 at.% of Fe-doped TiO_2 was less than that of 1 at.% of Fe-doped TiO_2. It was possible that it was the experiment error. The specific surface area of 1 and 5 at.% of Fe-doped TiO_2 decreased from 109 to 98 m^2/g, corresponded to BET equivalent diameters of 11 to 13 nm, respectively. The changing of specific surface area caused by the V^{4+}, Cu^{2+}, Fe^{3+} substitution in Ti^{4+} by forming solid solution. V^{4+}, Cu^{2+}, Fe^{3+} ions could be substituted in Ti^{4+} ion because the ionic radii of V^{4+}(0.61 Å), Cu^{2+}(0.59 Å), Fe^{3+}(0.64 Å) are similar to that of Ti^{4+}(0.68 Å). The specific surface area did not change due to the presence of Fe^{3+} on the catalysts surface as mentioned by Araña et al. [110]. However, the concomitant increase in crystallite size and changes in the structure with the decrease in surface area was postulated to greatly influence the photocatalytic property of the catalyst [59].

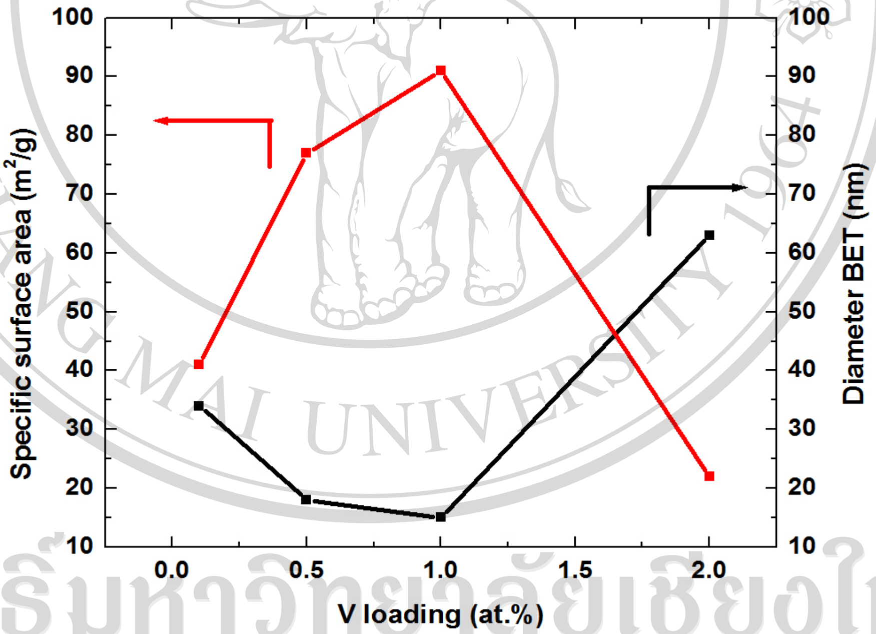

Figure 3.6 SSA and BET equivalent diameter of 0.1-2 at.% of V-doped TiO_2 prepared by the modified sol-gel method

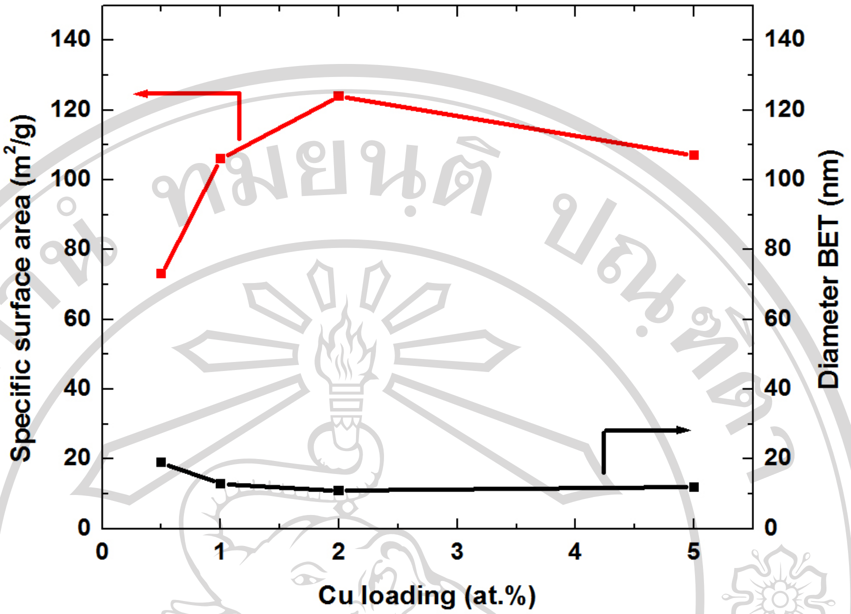

Figure 3.7 SSA and BET equivalent diameter of 0.5-5 at.% of Cu-doped TiO_2 prepared by the modified sol-gel method

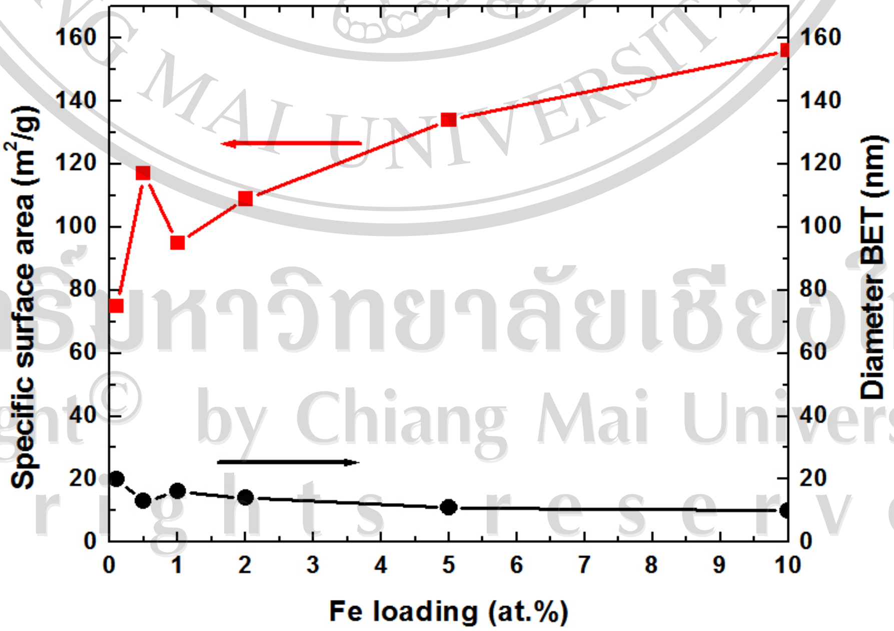

Figure 3.8 SSA and BET equivalent diameter of 0.1-10 at.% of Fe-doped TiO_2 prepared by the modified sol-gel method

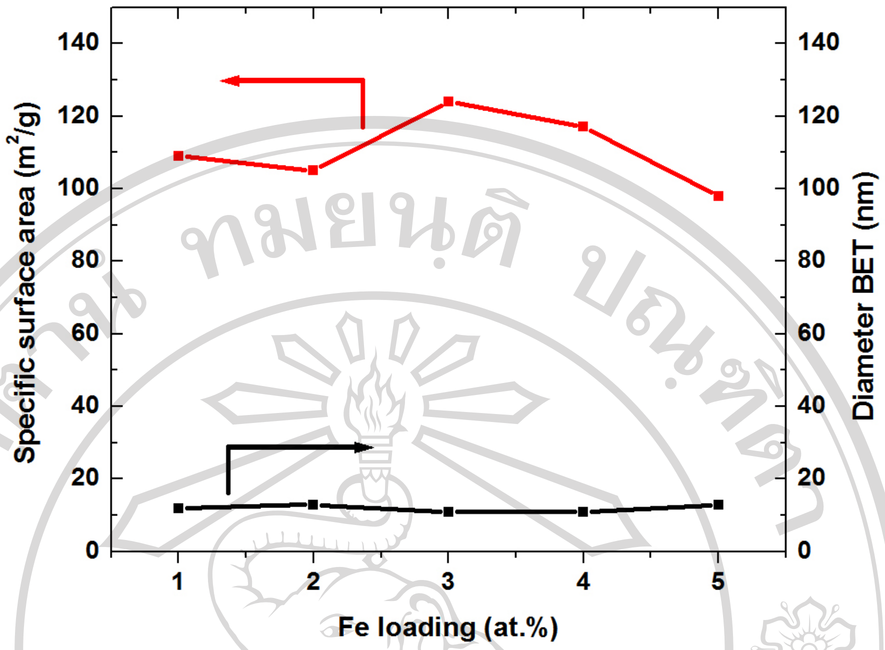

Figure 3.9 SSA and BET equivalent diameter of 1-5 at.% of Fe-doped TiO_2 prepared by the impregnation method

3.2.3 X-ray diffraction studies

Figure 3.10 shows the X-ray diffraction patterns of TiO_2 derived from the modified sol-gel method by heat treatment for 3h between 400 and 900 °C. XRD patterns of anatase TiO_2 indicated that the position and intensity of the characteristic peaks of the samples were confirmed with the JCPDS file no. 21-1272 at 400-900 °C. The rutile phase appeared in XRD peaks when calcined at the temperature of 800 °C and was confirmed with the JCPDS file no. 76-318. Therefore, it was confirmed that the anatase to rutile transformation state occurred at a temperature between 700 and 800 °C. All samples exhibited the characteristic peaks of mainly anatase phase, which became sharper as the calcination temperature increased. Decreasing of the width-half maximum of the main peak with an increase in the calcination temperature was indicated as an increase in crystallinity as well as an increase in the size of the particles. As shown in Figure 3.11, the anatase phase composition decreased linearly from 99 to 90 wt.% with the increasing of calcination temperatures. The particles sizes of anatase phase were increased from 15 to 108 nm as the calcination temperature changed from 400 to 900 °C, respectively. The rutile crystallite sizes and rutile phase content increased with high calcination temperature. However, very little rutile phase content was found to increase from 0.15 to 0.28 wt.% when increasing the temperature from 400 to 700 °C. Some reports proposed that anatase phase gave high photocatalytic activity in term of the degree of hydroxylation, while rutile was a very low density of hydroxyl groups on its surface [61, 62].

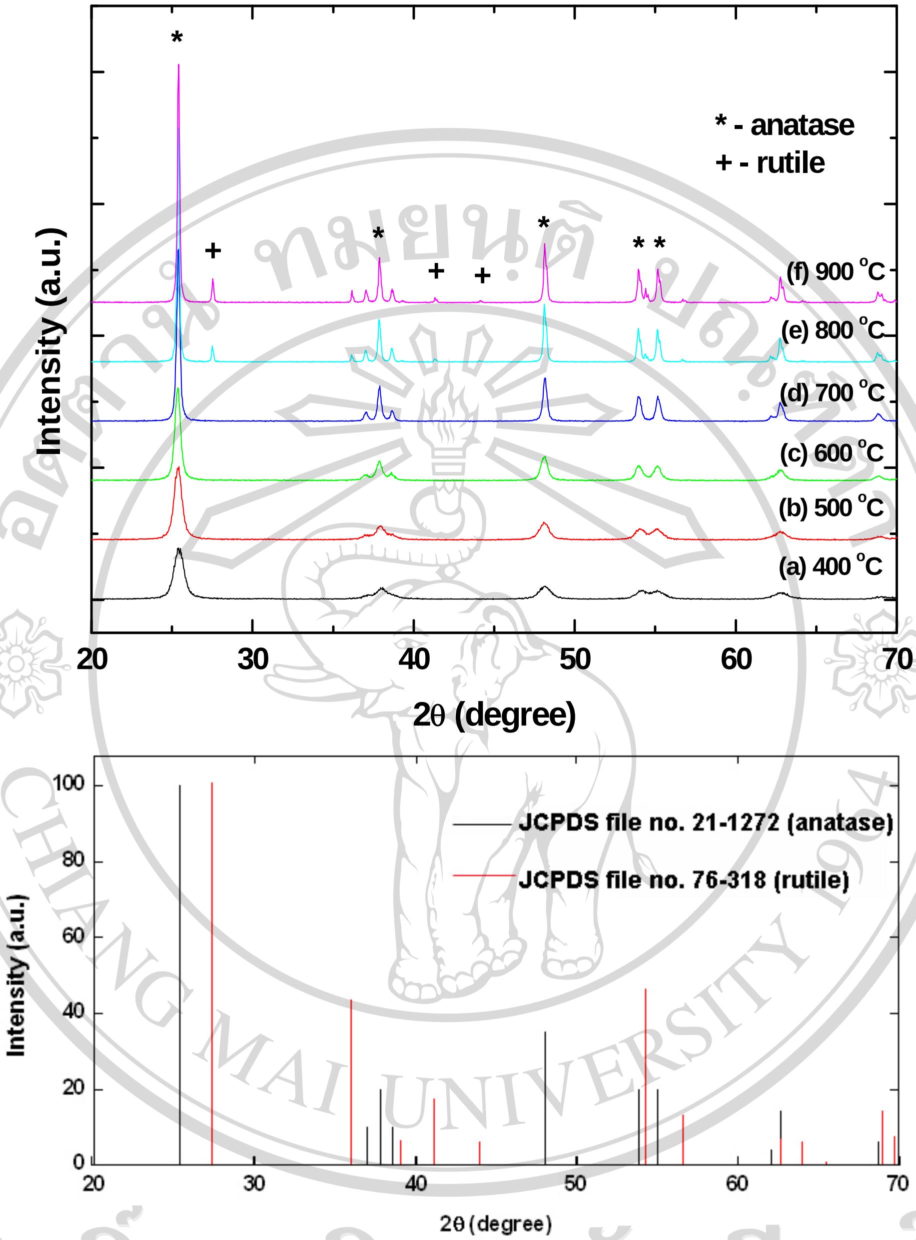

Figure 3.10 XRD patterns of pure TiO_2 prepared by the modified sol-gel method and subjected to heat treatment between 400-900 °C for 3h

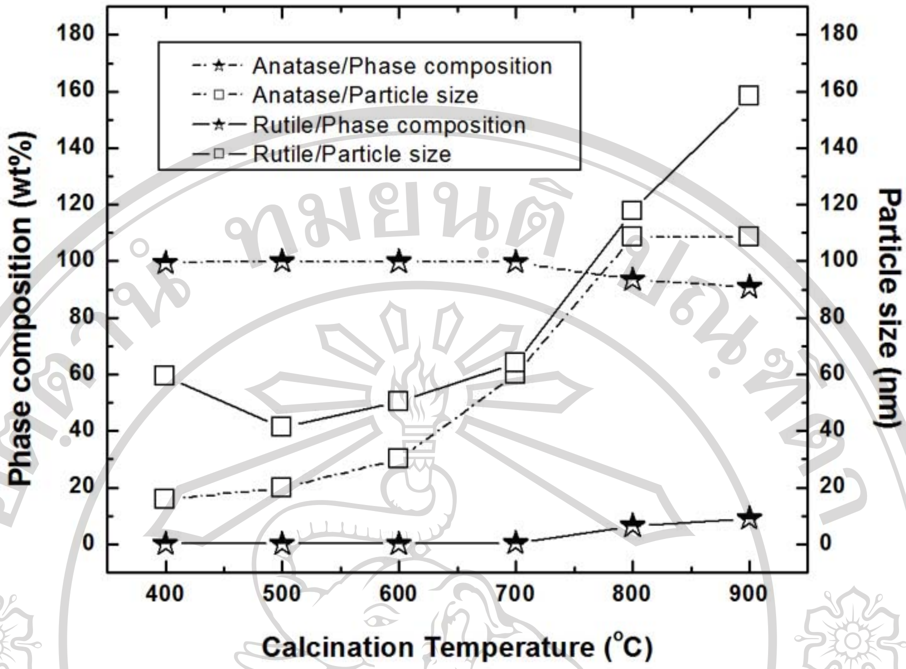

Figure 3.11 Effect of calcination temperature on phase composition and particle size TiO_2 prepared by the modified sol-gel method and subjected to heat treatment between 400-900 °C for 3h

XRD patterns of anatase TiO_2 and V, Cu, Fe-doped TiO_2 prepared by the modified sol-gel method and Fe-doped TiO_2 prepared by impregnation method were demonstrated that the position and intensity of characteristic peaks of the samples were conformed to the JCPDS file no. 21-1272. The XRD patterns of V, Cu, Fe-doped TiO_2 were identified to predominantly anatase phase as shown in Figure 3.12-3.15. When increased the amount of V, the peaks of diffraction pattern became sharper, it could be assumed to be due to the bigger particle sizes as shown in Figure 3.12. The sharper peaks and the broader peaks of XRD patterns were assumed to be due to the bigger particles and smaller particles, respectively. Moreover, the sharper and broader peaks could indicate the crystallinity in the samples. The sharper or broader peaks of XRD patterns could be related to the BET data. However, the characteristic of XRD peaks indicate roughly the particle size but the actual size of the particles was further investigated by TEM measurement later. The rutile phase was not present in the XRD patterns. The peaks of V, Fe, and Cu were not seen in XRD patterns due to their small amount of vanadium, copper, and iron in TiO_2 crystal. From the results, it could be concluded that V, Fe, and Cu did not have any effect on the anatase-rutile phase transformation of the titanium dioxide. Moreover, the ionic radii of V, Fe, Cu are similar to Ti which enable their substitutation in titanium ion. The diffraction peaks of Cu-doped TiO_2 as the amount of copper increased the grain size of Cu-doped TiO_2 particles became smaller as shown in Figure 3.13. In Figures 3.14 and 3.15 shows the diffraction patterns of Fe-doped TiO_2 prepared by the modified sol-gel method and the impregnation method, respectively. As the amount of iron increased, the diffraction peaks became broader due to the grain size of TiO_2 powder became smaller. However, the peak of 10 at.% Fe-doped TiO_2 became broader because the excessive amount of Fe doping disturbed the arrangement of the TiO_2 basic octahedral units and hence distorted the overall crystallite structure as mentioned by Teoh et al. [44]. No vanadium, iron, and copper containing phase could be resolved in these patterns, which suggested insignificant vanadium, iron, and copper segregation in the doped samples. Zhu et al. [109] explained that the substitution of iron ion in titanium ion depended on the different sizes of ionic radii of iron and titanium ions. The ionic radius of Fe^{3+} (0.64 Å), V^{4+} (0.61 Å), and Cu^{2+} (0. 59 Å) were smaller not more than Ti^{4+} (0.68 Å).

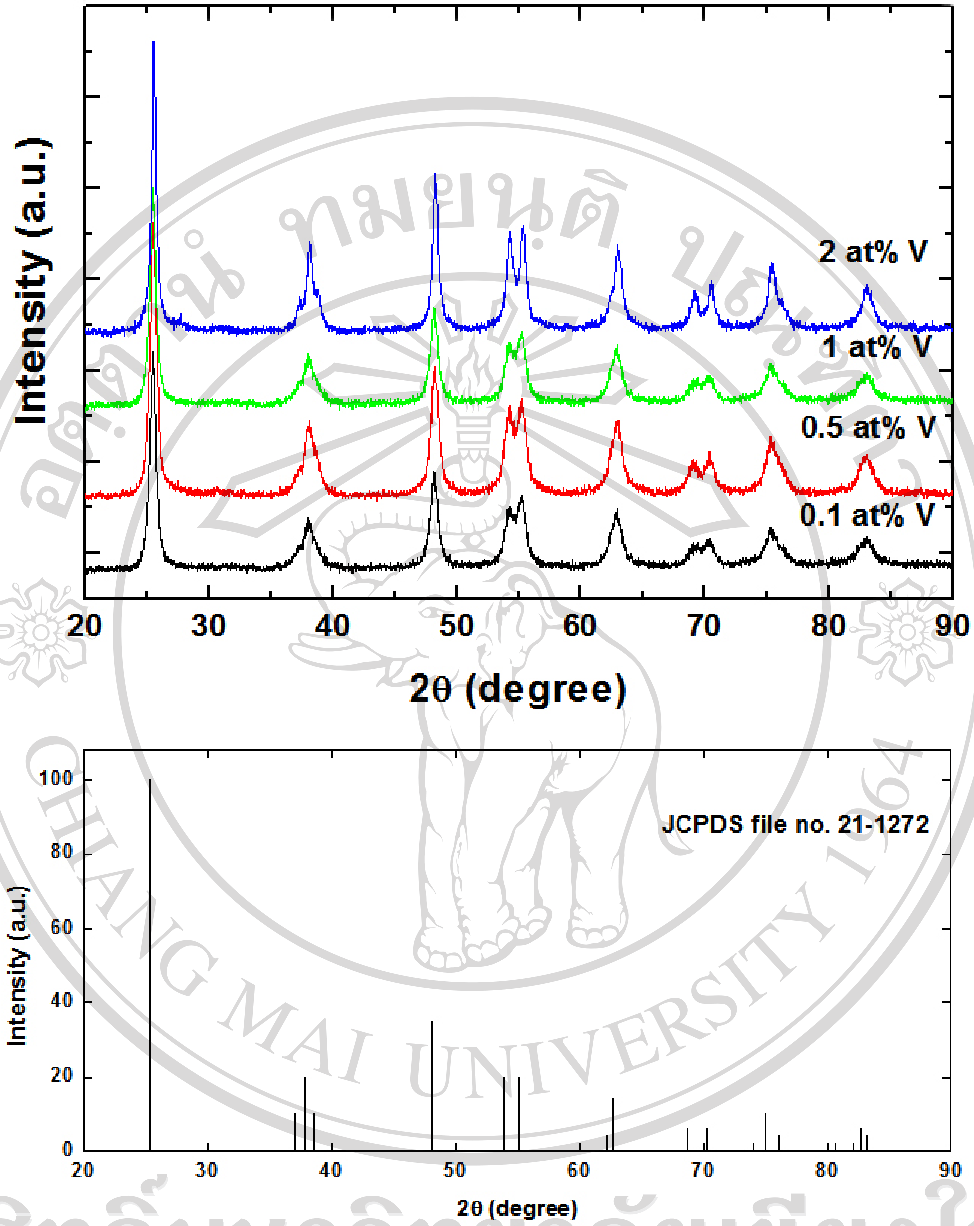

Figure 3.12 XRD patterns of 0.1-2 at.% of V-doped TiO_2 prepared by the modified sol-gel method at the calcination temperature of 400 °C for 3h

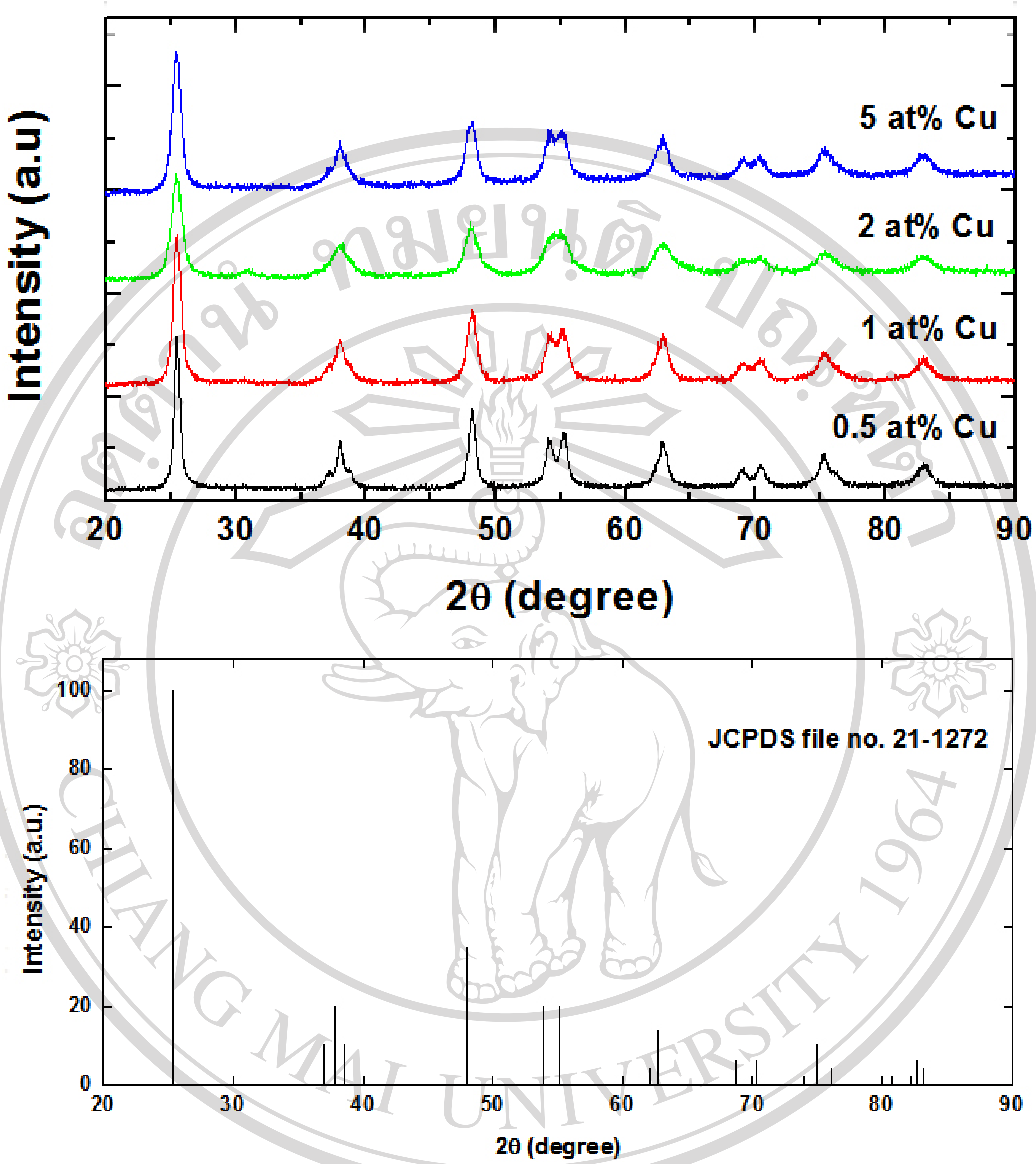

Figure 3.13 XRD patterns of 0.5-5 at.% of Cu-doped TiO_2 prepared by the modified sol-gel method at the calcination temperature of 400 °C for 3h

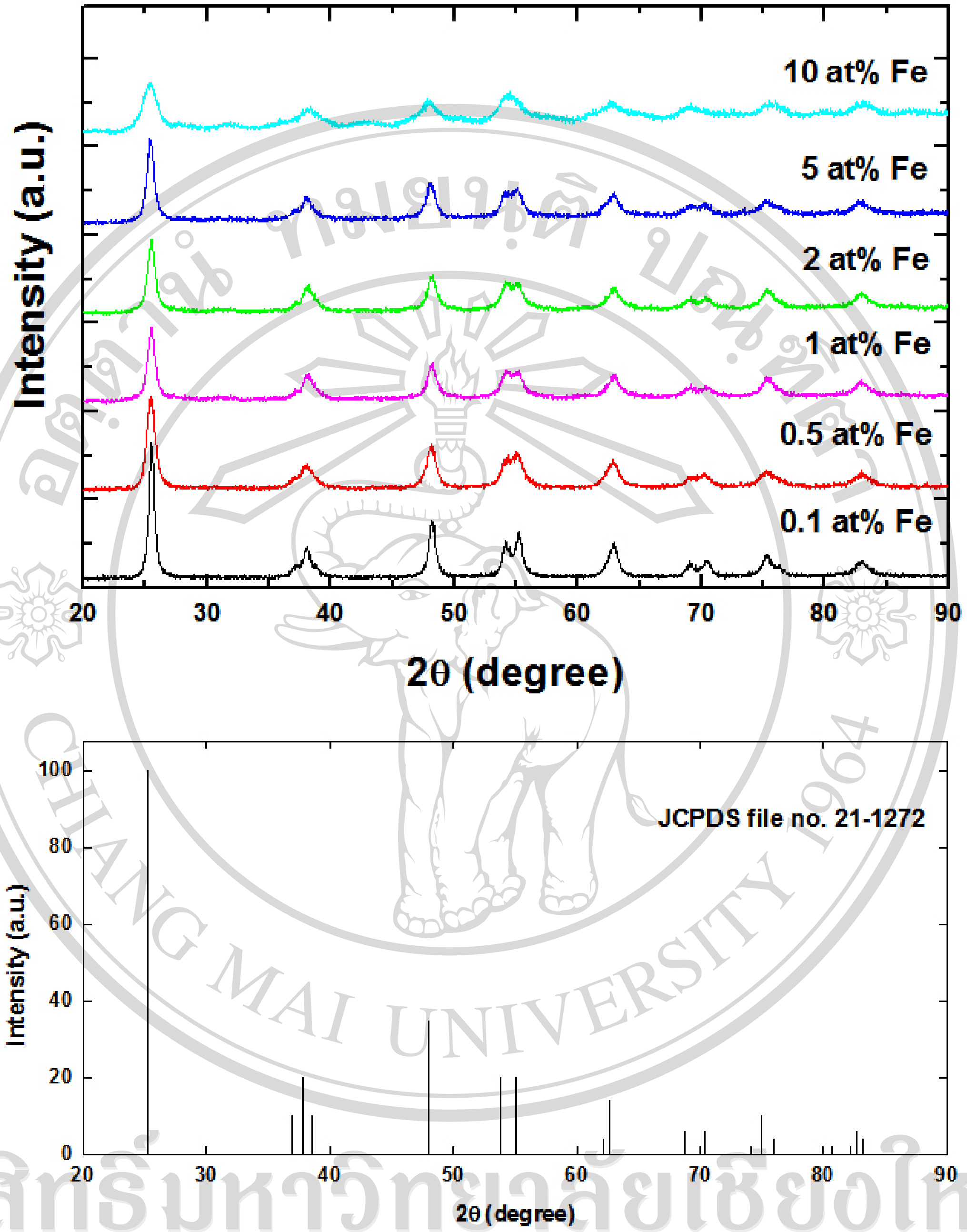

Figure 3.14 XRD patterns of and 0.1-10 at.% of Fe-doped TiO_2 prepared by the modified sol-gel method at the calcination temperature of 400 °C for 3h

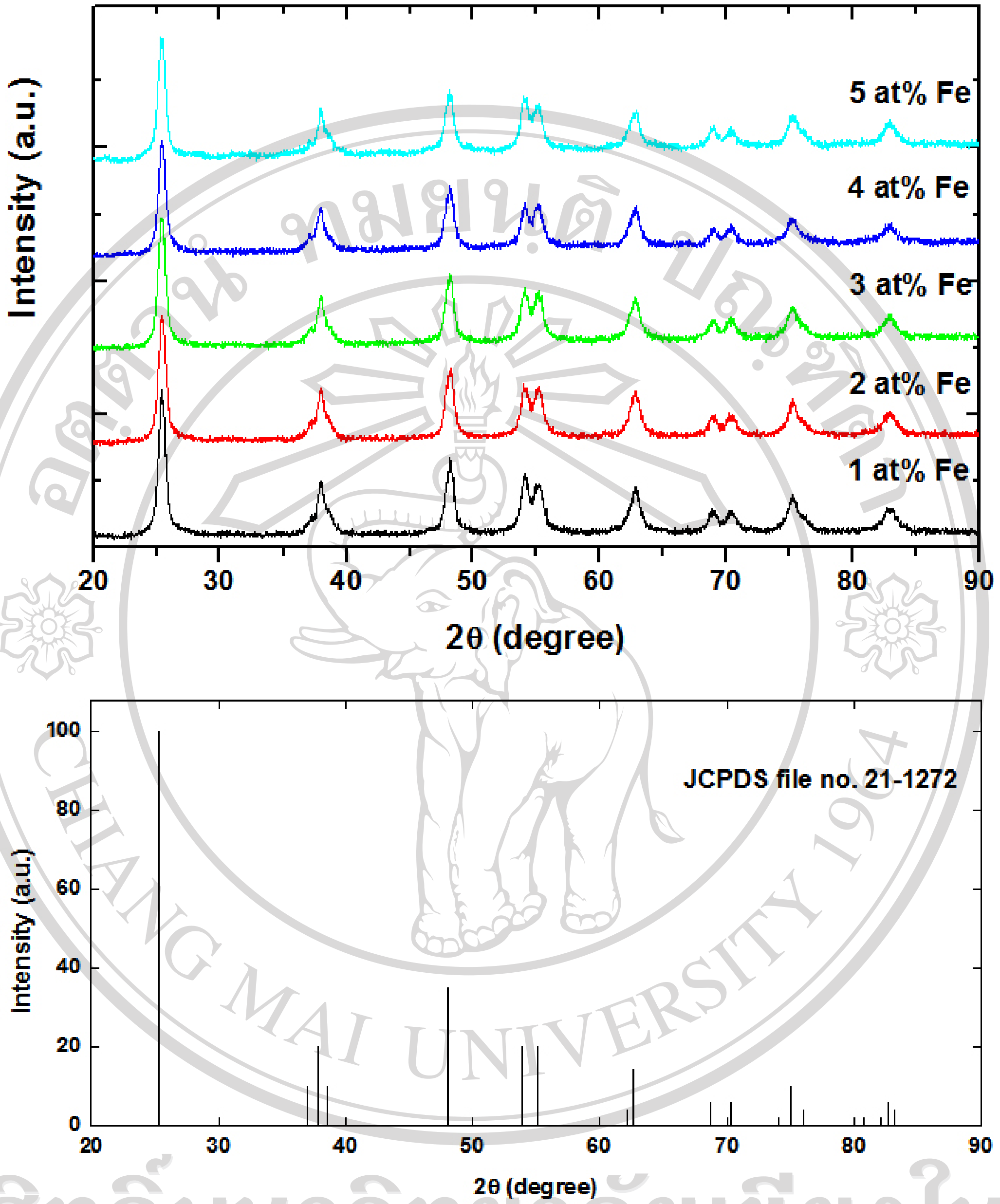

Figure 3.15 XRD patterns of 1-5 at.% of Fe-doped TiO_2 prepared by the impregnation method at the calcination temperature of 400 °C for 3h

3.2.4 Transmission electron microscopy studies

3.2.4.1 TEM of pure TiO_2 prepared by the modified sol-gel method

Figure 3.16 shows TEM images of pure TiO_2 in the anatase phase demonstrated that they had almost spherical shape. The average sizes of pure TiO_2 were in the range of 15-30 nm at calcination temperature between 400-600 ºC. Pure anatase TiO_2 was obtained at 400 ºC in the form of well crystallized small particles of 15 nm. The crystallite size of anatase increased as calcination temperature increased up to 700 ºC. It should be emphasized that the smaller particle size is an important parameter in photocatalytic reaction as it directly indicates the higher specific surface area of the catalyst.

Electron diffraction patterns showed the brightness of polymorphic discrete ring of the crystalline as shown in the insets of Figures 3.16(a), (b), (c), (d). The trend was corresponding to crystallographic data provided by Joint Committee Powder Diffraction Standards (JCPDS) Powder Diffraction File. Electron diffraction patterns could be determined lattice spacing from this equation $\lambda L=Rd$ where; λL (camera constant, 24.9630 mmÅ) and R is the radius from the center of the inner ring to the next ring. The lattice spacing of pure TiO_2 calcined at 400 °C for 3h calculated from electron diffraction pattern corresponded with JCPDS file no. 21-1272. It can be concluded that electron diffraction pattern corresponding with TiO_2 in XRD data. The corresponding spot ring type of diffraction pattern indicated that the crystals orientated in a number of different directions. The ring patterns of pure TiO_2 indicated quite high degree of crystallinity and in polycrystal.

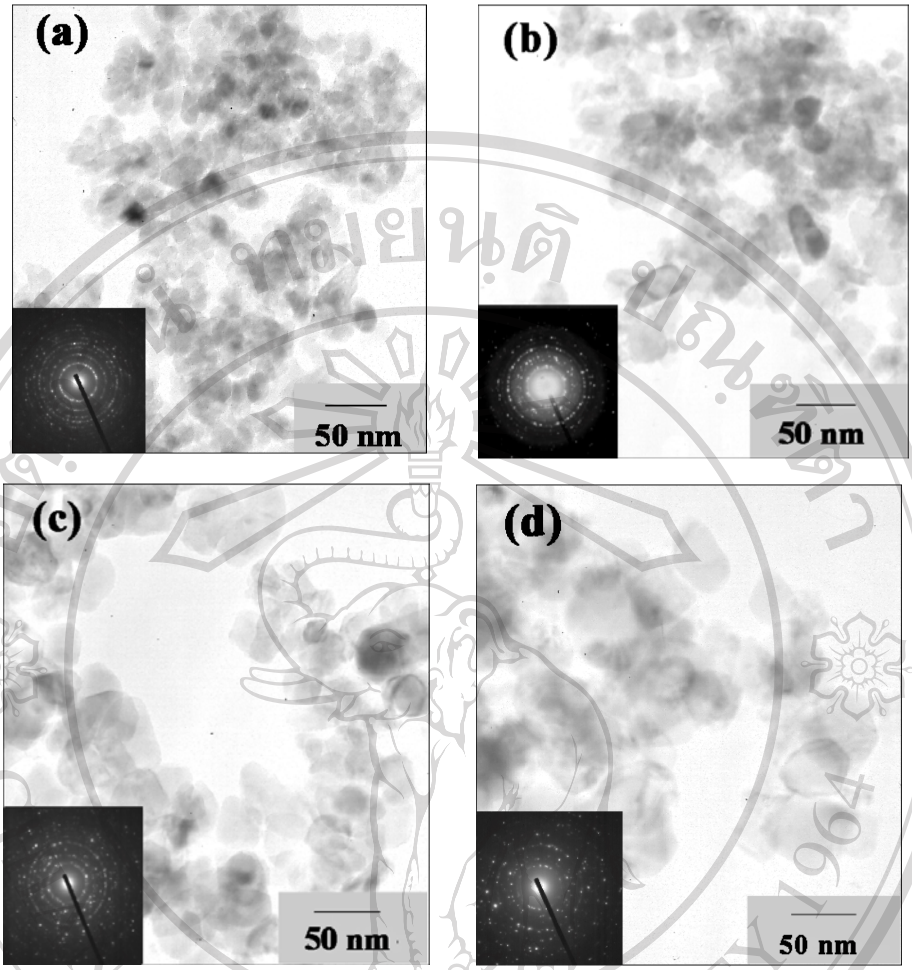

Figure 3.16 TEM images of pure TiO_2 prepared by the modified sol-gel method and subjected to heat treatment at (a) 400 °C (b) 500 °C (c) 600 °C (d) 700 °C for 3h, respectively. Insets show the corresponding diffraction patterns of pure TiO_2.

3.2.4.2 TEM of V-doped TiO_2 prepared by the modified sol-gel method

Figure 3.17 shows TEM images of the V-doped TiO_2 (0.1 and 0.5 at.%) in the anatase phase demonstrated that they had almost spherical shape. The average particle sizes of 0.1 and 0.5 at.% V-doped TiO_2 were in the range of 15-20 nm at calcination temperature of 400 ºC for 3h. The lattice spacing of V-doped TiO_2 calcined at 400 °C for 3h calculated from electron diffraction patterns corresponded with JCPDS file no. 21-1272. It can be concluded that electron diffraction patterns corresponds with TiO_2 in XRD data. The ring patterns of V-doped TiO_2 indicated quite high degree of crystallinity and in polycrystalline phase. The particle sizes of 0.1 and 0.5 at.% V-doped TiO_2 obtained from TEM measurement were not much different from the BET equivalent diameter. The particle sizes of 0.1 and 0.5 at.% V-doped TiO_2 were found in the range of 15-20 while BET equivalent diameters were found to be 30 nm. However, the BET equivalent diameters of V-doped TiO_2 obtained from BET calculation were bigger than the size obtained from TEM measurement due to the agglomeration of particles which affected the surface area. The square areas selected emphasized for the EDS investigation with chemical elements of V-doped TiO_2 as shown in Figure 3.17(a) and (b). EDS spectrum of chemical elements of 0.1 and 0.5 at.% of V-doped TiO_2 (Table 3.1) were analyzed from EDS spectra as shown in Figures 3.18(a) and 3.18(b), respectively. Although Cu was detected, the Cu signal arose from the background support of carbon-coated copper grid. The element composition data from EDS confirmed vanadium was actually in V-doped TiO_2. However, the amount of element composition was slightly different depending on the different selected area of EDS analysis

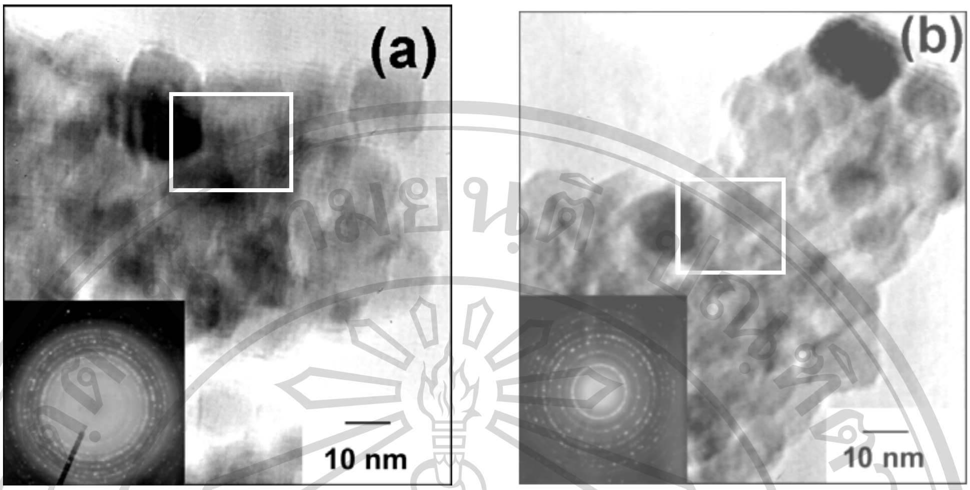

Figure 3.17 TEM micrographs of (a) 0.1 at.% of V, and (b) 0.5 at.% of V-doped TiO_2 prepared by the modified sol-gel method. The square areas were the selected area emphasized for the EDS investigation with chemical elements of V-doped TiO_2.

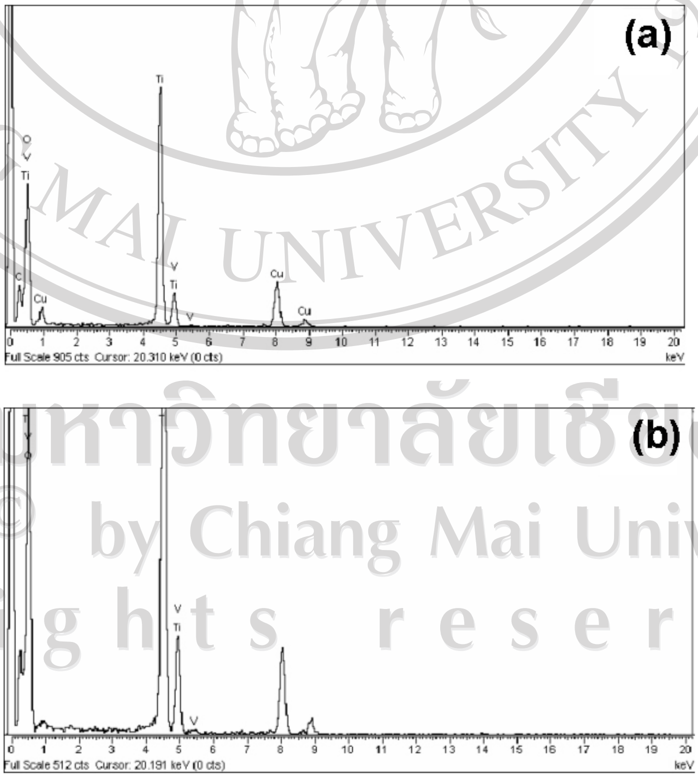

Figure 3.18 EDS analysis of (a) 0.1 at.% of V and (b) 0.5 at.% of V-doped TiO_2

Table 3.1 Relation between elements and atomic% of V-doped TiO_2

Samples	Element (at.%)			
	O	Ti	V	Total
0.1 at.% V-doped TiO_2	61.379	38.046	0.565	100.00
0.5 at.% V-doped TiO_2	61.075	37.023	1.902	100.00

3.2.4.3 TEM of Cu-doped TiO_2 prepared by the modified sol-gel method

TEM images of 0.5, 1, and 2 at.% of Cu-doped TiO_2 in the anatase phase demonstrated their almost spherical shape as shown in Figure 3.19. The average particle sizes of 0.5-2 at.% Cu-doped TiO_2 were in the range of 10-20 nm at calcination temperature of 400 ºC. The crystalline sizes decreased with increasing amount of copper doping. The particle sizes of 0.5, 1, 2 at.% Cu-doped TiO_2 obtained from TEM measurement matched well with the BET equivalent diameter (11-19 nm). The lattice spacing of Cu-doped TiO_2 calcined at 400 °C for 3h calculated from electron diffraction patterns corresponded with JCPDS file no. 21-1272. It can be concluded that electron diffraction patterns corresponds with TiO_2 in XRD data. The ring patterns of Cu-doped TiO_2 indicated quite high degree of crystallinity and in polycrystalline phase. Copper could not be detected from EDS analysis because the specimen was made from carbon-coated copper grid. The amount of copper was confirmed with EDS mapping mode in SEM instrument in the next section.

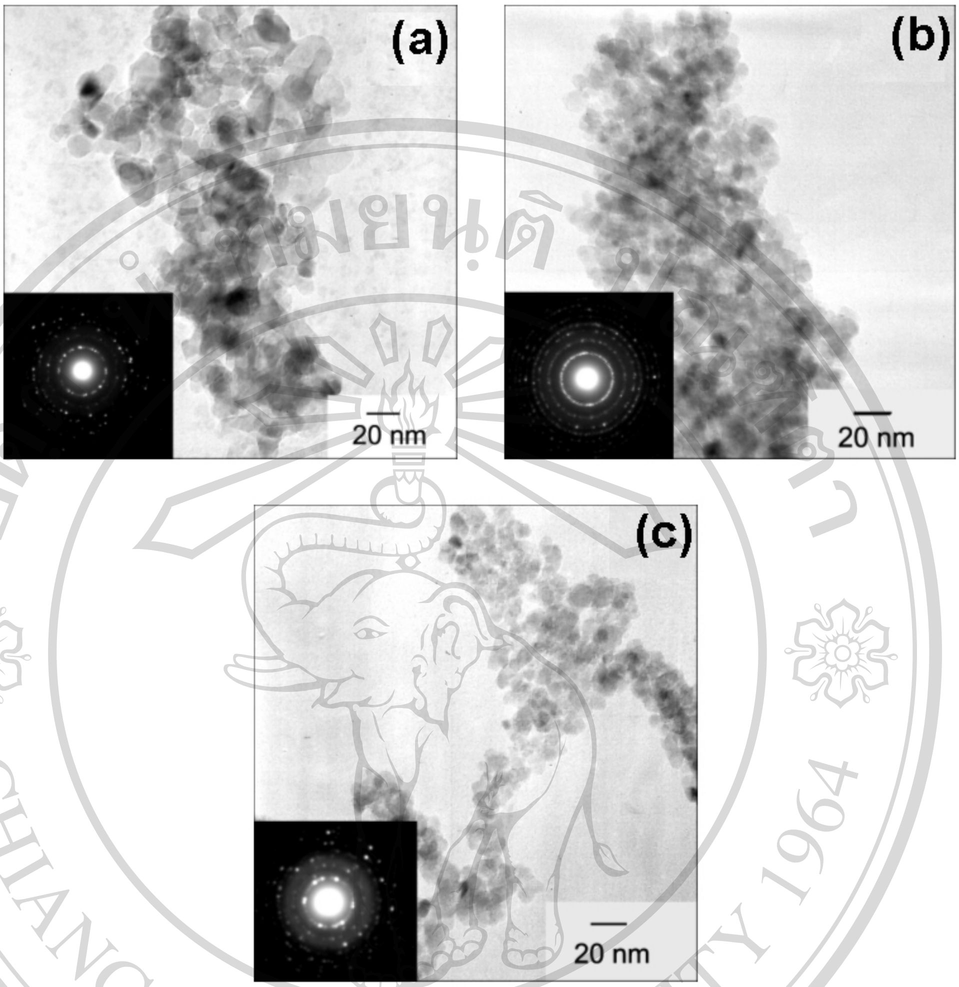

Figure 3.19 TEM micrographs of (a) 0.5 at% of Cu, (b) 1 at% of Cu, and (c) 2 at% of Cu-doped TiO_2 prepared by the modified sol-gel method

3.2.4.4 TEM of Fe-doped TiO_2 prepared by the modified sol-gel method

TEM images of 0.5, 1, 2, 5 at.% of Fe-doped TiO_2 in the anatase phase demonstrated the almost spherical shape as shown in Figure 3.20. The average particle sizes of 0.5, 1, 2, 5 at.% Fe-doped TiO_2 were in the range of 15-20 nm at calcination temperature of 400 ºC for 3h. The particle sizes of 0.5, 1, 2, 5 at.% Fe-doped TiO_2 obtained from TEM measurement matched well with the BET equivalent diameter of 10-20 nm obtained from BET calculation. The lattice spacing of Fe-doped TiO_2 calcined at 400 °C for 3h calculated from electron diffraction patterns corresponded with JCPDS file no. 21-1272. It can be concluded that electron diffraction patterns corresponds with TiO_2 in XRD data. The ring patterns of Fe-doped TiO_2 indicated quite high degree of crystallinity and in polycrystalline phase. The square areas selected emphasized for the EDS investigation with chemical elements of Fe-doped TiO_2 as shown in Figure 3.20(a), (b), (c), and (d). EDS spectrum of chemical elements of 0.5, 1, 2, 5 at.% of Fe-doped TiO_2 (Table 3.2) were analyzed from EDS spectra as shown in Figures 3.21 (a), (b), (c), and (d), respectively. The EDS spectrum of Fe-doped TiO_2 showed the existence of Fe dopant and the Cu spectra came from carbon-coated copper grid. The amount of iron doping depends on the selected area of EDS analysis.

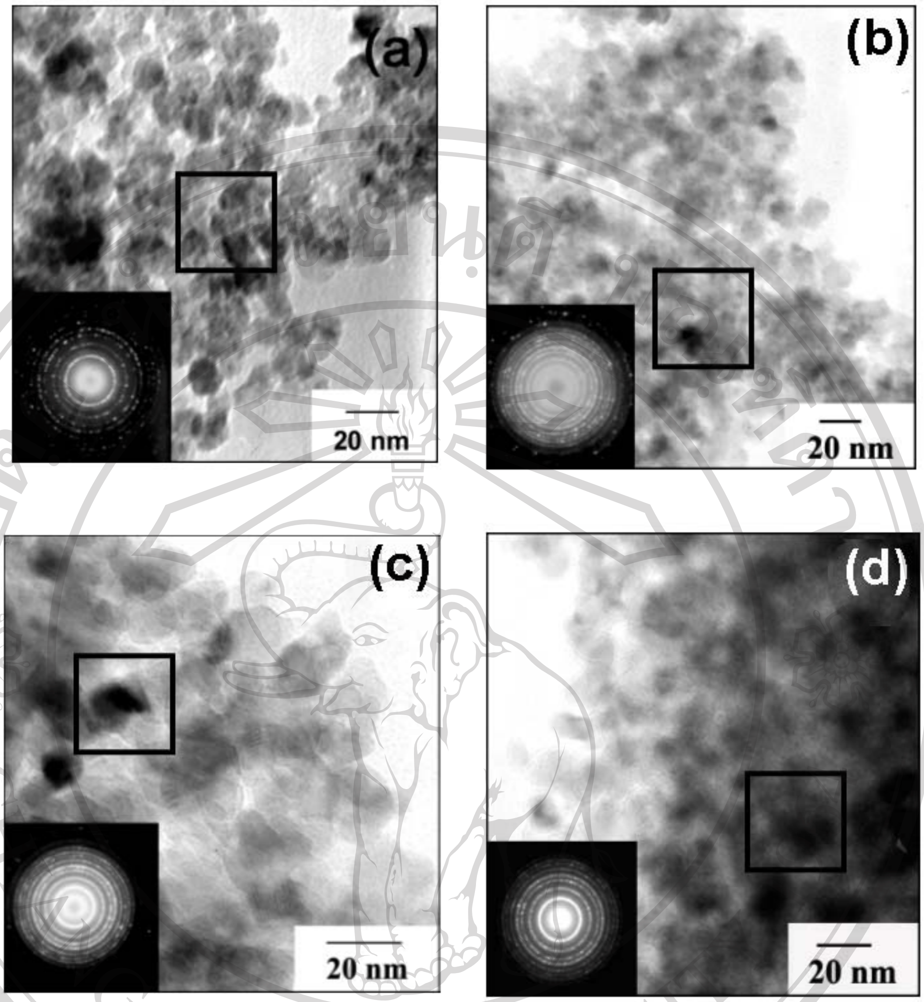

Figure 3.20 TEM micrographs of (a) 0.5 at.% of Fe, (b) 1 at.% of Fe, (c) 2 at.% of Fe, and (d) 5 at.% of Fe-doped TiO_2 prepared by the modified sol-gel method. The square areas selected emphasized for the EDS investigation with chemical elements of Fe-doped TiO_2.

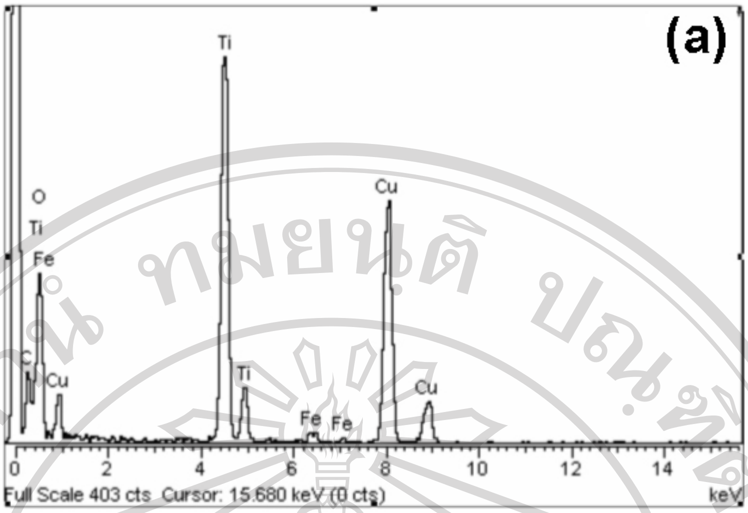
(a)
Ti
O
Ti
Fe
C
Cu
Ti
Cu
Fe
Fe
Cu
0
2
4
6
8
10
12
14
Full Scale 403 cts Cursor: 15.680 keV (0 cts)
keV

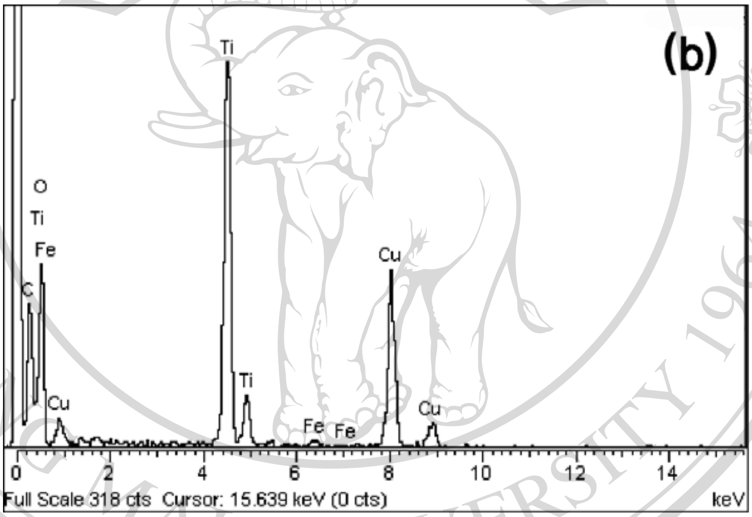
(b)
Ti
O
Ti
Fe
C
Cu
Ti
Cu
Fe
Fe
Cu
0
2
4
6
8
10
12
14
Full Scale 318 cts Cursor: 15.639 keV (0 cts)
keV

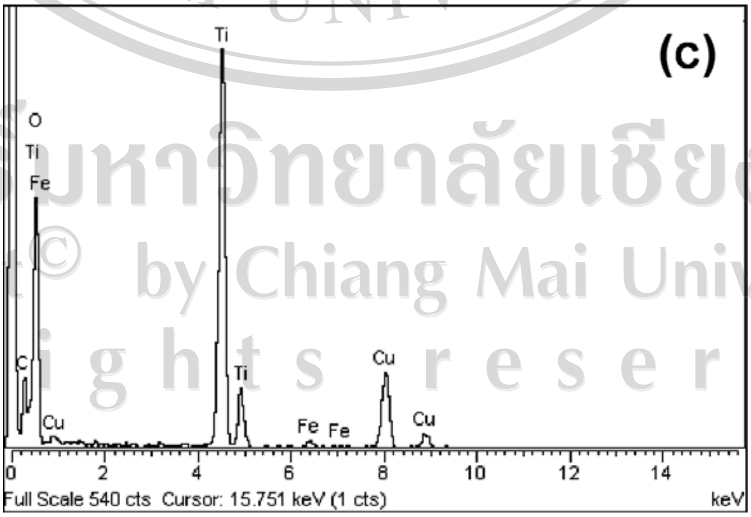
(c)
Ti
O
Ti
Fe
C
Cu
Ti
Cu
Fe
Fe
Cu
0
2
4
6
8
10
12
14
Full Scale 540 cts Cursor: 15.751 keV (1 cts)
keV

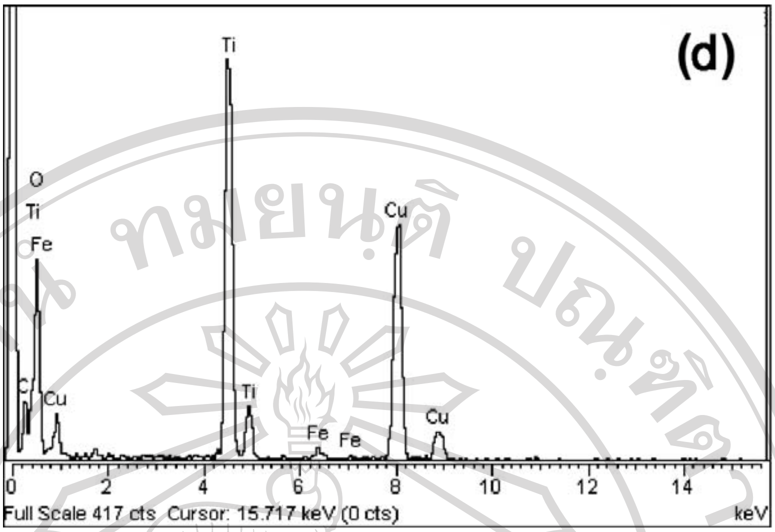

Figure 3.21 EDS analysis of (a) 0.5 at.% of Fe, (b) 1 at.% of Fe, (c) 2 at.% of Fe, and (d) 5 at.% of Fe-doped TiO_2

Table 3.2 Relation between elements and atomic% of Fe-doped TiO_2

Samples	Element (at.%)			
	O	Ti	Fe	Total
0.5 at.% Fe-doped TiO_2	61.08	38.74	0.18	100.00
1 at.% Fe-doped TiO_2	56.51	42.96	0.52	100.00
2 at.% Fe-doped TiO_2	63.80	35.70	0.50	100.00
5 at.% Fe-doped TiO_2	54.97	44.05	0.96	100.00

3.2.4.5 TEM of Fe-doped TiO_2 prepared by the impregnation method

TEM images of 1, 2, 3, 4, 5 at.% of Fe-doped TiO_2 in the anatase phase prepared by the impregnation method demonstrated the almost spherical shape as shown in Figure 3.22. The average particle sizes of 1, 2, 3, 4, 5 at.% Fe-doped TiO_2 were in the range of 10-20 nm at calcination temperature of 400 ºC for 3h. The particle sizes of 1, 2, 3, 4, 5 at.% Fe-doped TiO_2 obtained from TEM measurement matched well with the BET equivalent diameter of 11-13 nm. The lattice spacing of Fe-doped TiO_2 calcined at 400 °C for 3h calculated from electron diffraction patterns corresponded with JCPDS file no. 21-1272. It can be concluded that electron diffraction patterns corresponds with TiO_2 in XRD data. The ring patterns of Fe-doped TiO_2 indicated quite high degree of crystallinity and in polycrystalline phase. The square areas selected emphasized for the EDS investigation with chemical elements of Fe-doped TiO_2 as shown in Figure 3.22(a), (b), (c), and (d). EDS spectrum of chemical elements of 2, 3, 4, 5 at.% of Fe-doped TiO_2 (Table 3.3) were analyzed from EDS spectra as shown in Figures 3.23(a), (b), (c) and (d), respectively. Nevertheless, the elements of 1 at.% Fe-doped TiO_2 could not be detected by using EDS in TEM instrument because small amount of Fe-doped TiO_2 was present. The EDS spectrum of Fe-doped TiO_2 showed the existence of Fe dopant and the Cu spectra came from carbon-coated copper grid. The element composition data from EDS confirmed iron was actually in Fe-doped TiO_2. However, the amount of elemental composition was slightly different depending on the different selected spot of EDS analysis.

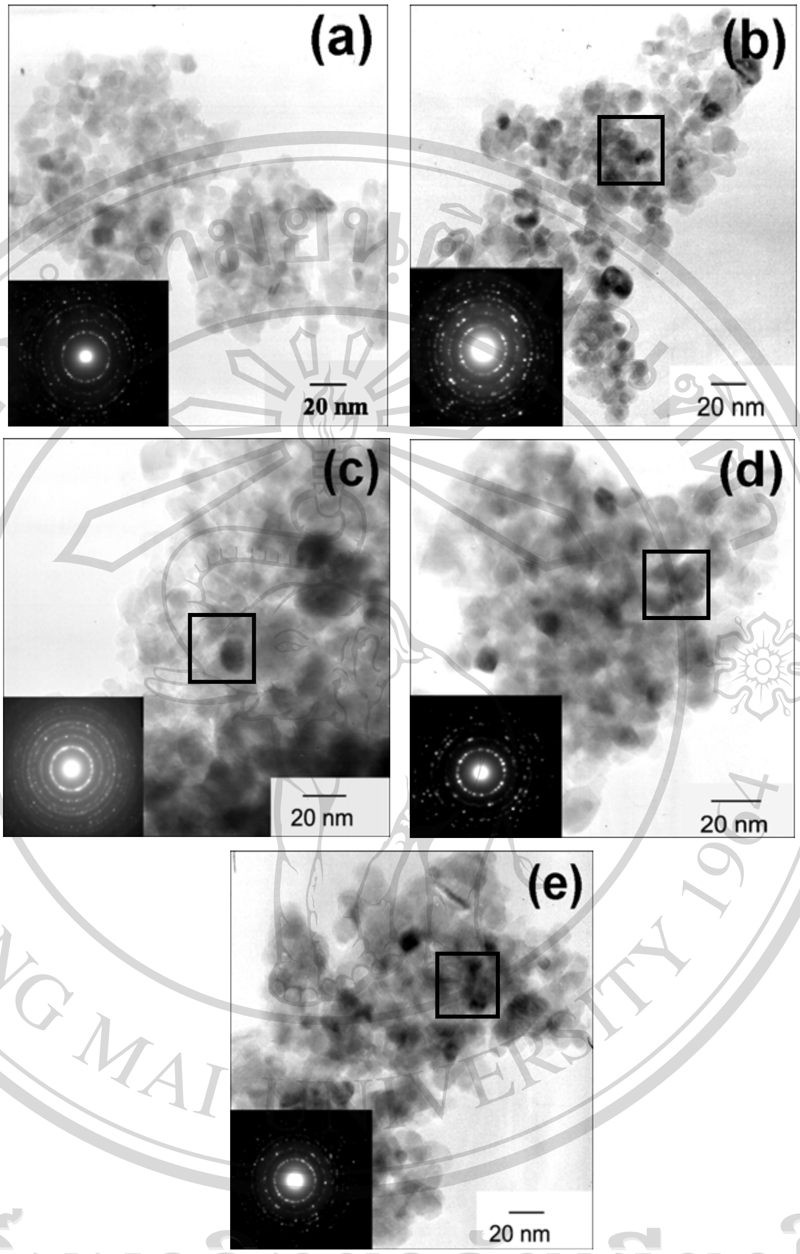

Figure 3.22 TEM micrographs of (a) 1 at% of Fe, (b) 2 at% of Fe, (c) 3 at% of Fe, (d) 4 at% of Fe, and (e) 5 at% of Fe-doped TiO_2 prepared by the impregnation method. The square areas selected emphasized for the EDS investigation with chemical elements of Fe-doped TiO_2.

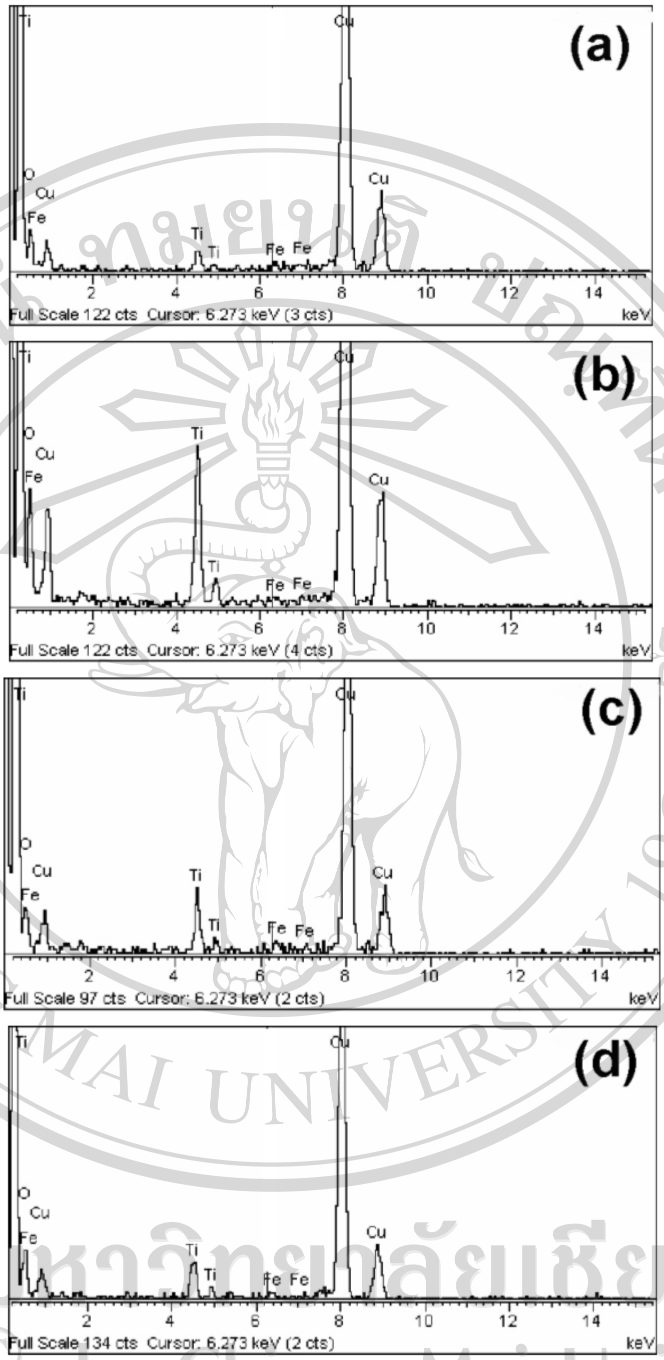

Figure 3.23 EDS analysis of (a) 2 at.% of Fe, (b) 3 at.% of Fe, (c) 4 at.% of Fe, (d) 5 at.% of Fe-doped TiO_2

The samples prepared by the modified sol-gel method and the impregnation method have the uniform small particle sizes, high specific surface area, which was favorable for high photocatalytic activity. The impregnation method has many advantages such as the actual amount of iron on TiO_2 could be prepared and the ease in preparing the doped catalysts. It could be seen from dark reddish color of Fe-doped TiO_2 prepared by the impregnation method at the same amount of iron dopant when compared with color of Fe-doped TiO_2 prepared by the modified sol-gel method.

Table 3.3 Relation between elements and atomic% of Fe-doped TiO_2 prepared by the impregnation method

Samples	Element (at.%)			
	O	Ti	Fe	Total
2 at.% Fe-doped TiO_2	63.289	32.621	4.089	100.00
3 at.% Fe-doped TiO_2	55.986	43.693	0.326	100.00
4 at.% Fe-doped TiO_2	36.334	54.867	8.800	100.00
5 at.% Fe-doped TiO_2	62.376	33.858	3.767	100.00

3.2.5 Scanning electron microscopy studies

The copper element on 0.5 at.% Cu-doped TiO_2 powders were not confirmed by using EDS in TEM measurement. This was due to the contamination from the copper grid coated with carbon. Therefore, the EDS technique could be considered for the measurement copper element on carbon tape. SEM image and EDS mapping mode of the Cu-doped TiO_2 sample are shown in Figure 3.24. The elemental compositions and particle distribution of 0.5 at.% Cu-doped TiO_2 were clearly confirmed from EDS mapping mode. The amount of Ti, O, and Cu elements were found to be 23.22, 75.81, and 0.96 at.%, respectively. EDS mapping mode showed good distribution of Ti, O, and Cu elements. The gold element on EDS mapping mode came from the coated gold before SEM measurement. The SEM images showed the crystallite size and morphology in a rough scale measurement. The morphology of Cu-doped TiO_2 was found to be not-so-hard-grained clusters and consisted of nearly spherical particles with diameters ranging from 100-200 nm. Although SEM images gave a rough estimate of particle sizes, TEM images can reveal internal structure and a more accurate measurement of particle sizes and morphology.

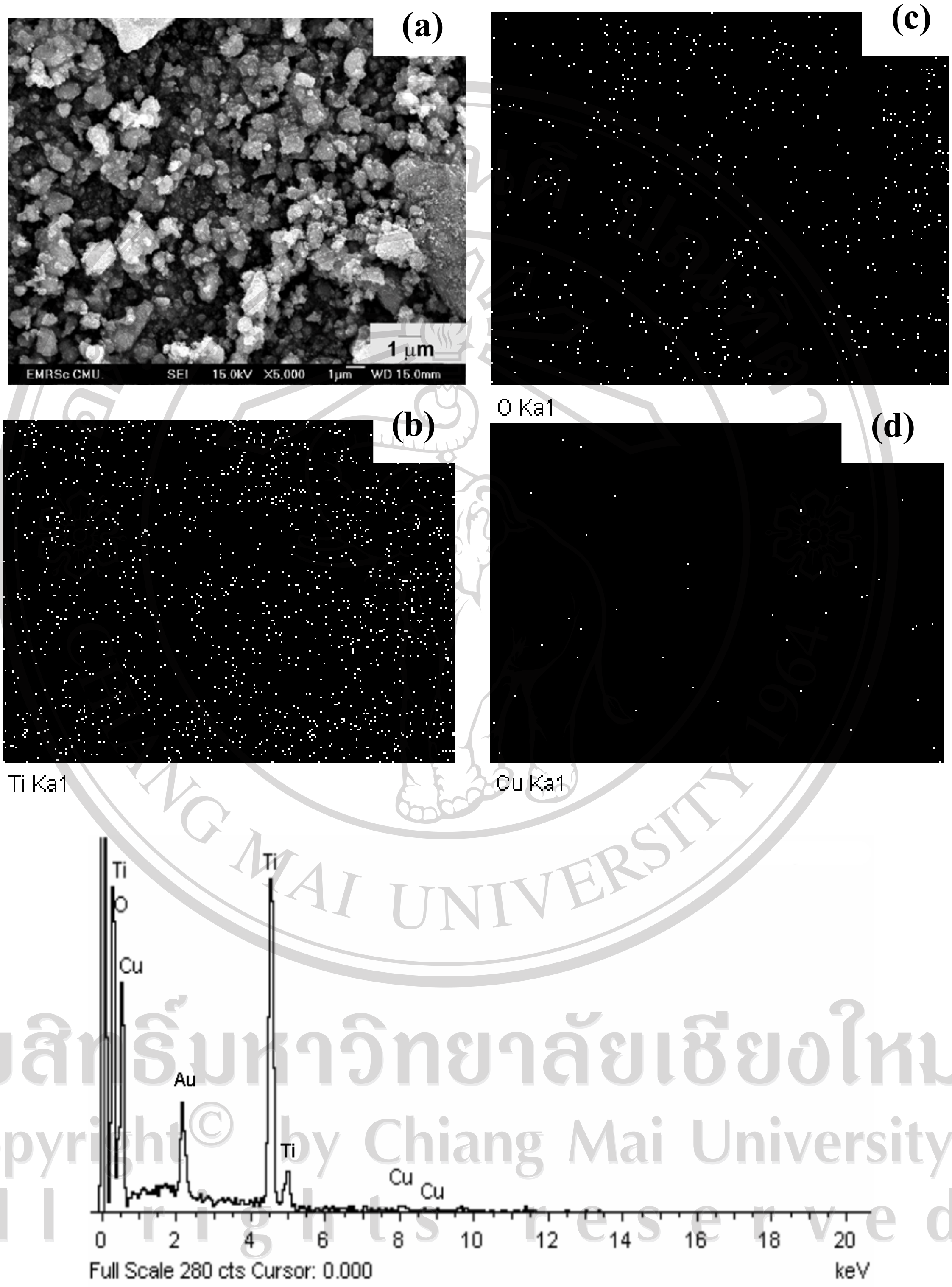

Figure 3.24 (a) SEM micrograph and EDS mapping mode of 0.5 at.% Cu-doped TiO_2 (b) Ti, (c) O, and (c) Cu elements

3.2.6 X-ray photoelectron spectroscopy (XPS) studies

Table 3.4 shows XPS binding energies (eV) of pure TiO_2, 2 at.% Fe-doped TiO_2, 0.5 at.% Cu-doped TiO_2 prepared by the modified sol-gel method and the impregnation method.

Table 3.4 XPS binding energies (eV) of pure TiO_2, 2 at.% Fe-doped TiO_2, 0.5 at.% Cu-doped TiO_2

Catalyst	**Binding Energy (eV)**					
	O 1s	**Ti $2p_{3/2}$**	**Ti $2p_{1/2}$**	**Fe $2p_{3/2}$**	**Fe $2p_{1/2}$**	**Cu**
Pure TiO_2 (sol-gel)	529.75 532.38	458.50	464.18	-	-	
0.5 at.% of Cu-doped TiO_2 (sol-gel)	529.72 531.87	458.42	464.12 460.70	-	-	-
2 at.% of Fe-doped TiO_2 (sol-gel)	529.69 531.56	458.73 458.21	464.21	709.72	-	-
2 at.% of Fe-doped TiO_2 (impregnation)	529.53 532.18	458.27	463.92	709.99	-	-

3.2.6.1 XPS of pure TiO_2 prepared by the modified sol-gel method

Pure TiO_2 prepared using titanium tetraisopropoxide as a precursor showed the binding energy of Ti and O as shown in Figure 3.25. XPS results of the binding energy, of the most intense peaks for various samples were listed in Table 3.4. The Ti $2p_{3/2}$ and Ti $2p_{1/2}$ binding energies for pure TiO_2 were found at 458.50 eV and 464.18 eV, respectively. The peaks were characterized by a narrow width which indicated that the Ti existed as Ti^{4+}. Fitting of the oxygen region produced two O 1s peaks, one at about 529.75 eV and another at about 532.38 eV corresponding to O^{2-} in the TiO_2 lattice and OH^- from surface hydroxyl groups or chemisorbed water molecules, respectively.

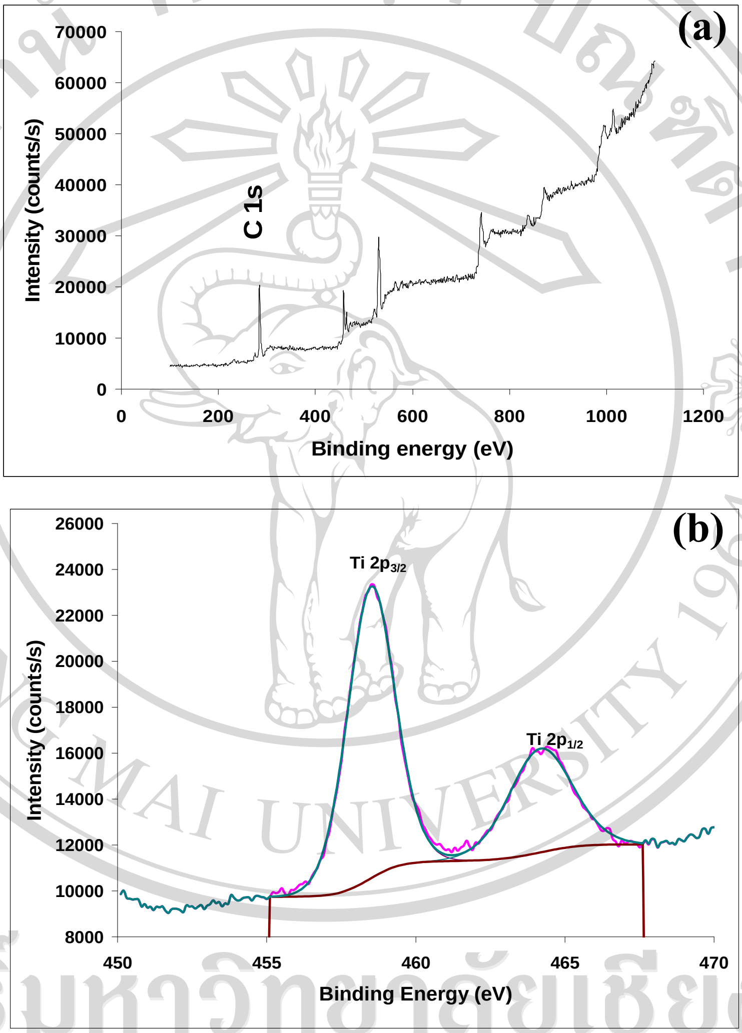

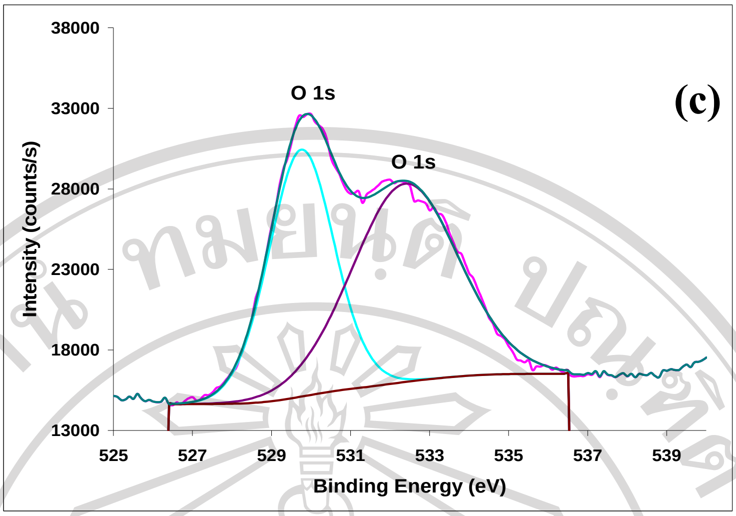

Figure 3.25 XPS spectra of pure TiO_2 (a) survey, (b) Ti 2p peaks, and (c) O 1s peaks

3.2.6.2 XPS of 0.5 at.% Cu-doped TiO_2 prepared by the modified sol-gel method

XPS was selected to determine the elemental surface compositions and oxidation state of elements of Cu-doped TiO_2, as shown in Figure 3.26. XPS results of the binding energy, of the most intense peaks for various samples were listed in Table 3.4. The Ti $2p_{3/2}$ and Ti $2p_{1/2}$ binding energies for Cu-doped TiO_2 were found at 458.42, and 464.12, 460.70, respectively. The peaks were characterized by a narrow width which indicated that the Ti existed as Ti^{4+}. Fitting of the oxygen region produced two O 1s peaks, one at about 529.72 eV and another at about 531.87 eV corresponding to O^{2-} in the TiO_2 lattice and OH^- from surface hydroxyl groups or chemisorbed water molecules, respectively. The binding energy of Cu element could not be detected by fitting the XPS measurement because little amount of Cu in the sample was limited.

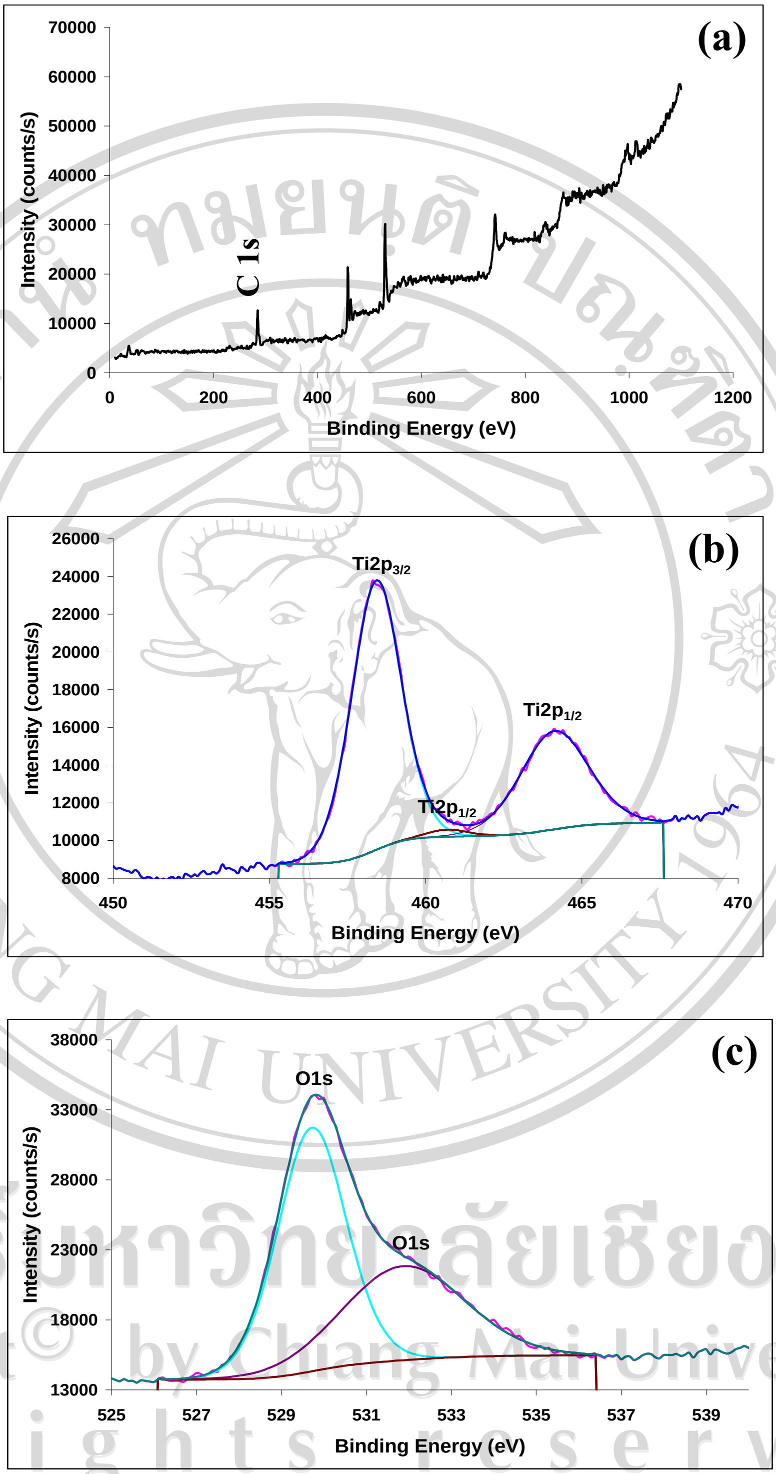

Figure 3.26 XPS spectra of 0.5 at.% of Cu-doped TiO_2 (a) survey, (b) Ti 2p peaks, and (c) O 1s

3.2.6.3 XPS of 2 at.% of Fe-doped TiO_2 prepared by the modified sol-gel method

XPS was selected to determine the elemental surface compositions and oxidation state of elements, as shown in Figure 3.27. XPS results of the binding energy, of the most intense peaks for various samples were listed in Table 3.4. The Ti $2p_{3/2}$ and Ti $2p_{1/2}$ binding energies for pure TiO_2 and 2 at.% of Fe-doped TiO_2 were found at 458.50 eV, 464.18 eV and 458.73, 464.21, respectively. The peaks were characterized by a narrow width which indicated that the Ti existed as Ti^{4+}. Fitting of the oxygen region produced two O 1s peaks, one at about 529 eV and another at about 531 eV corresponding to O^{2-} in the TiO_2 lattice and OH^- from surface hydroxyl groups or chemisorbed water molecules, respectively. Fe-doped TiO_2 samples were characterized by the binding energy Fe $2p_{3/2}$ equal to 709.72 eV typical of Fe^{3+} [111]. The slight enhancement of Fe 2p into TiO_2 lattice indicated the formation of Fe-O-Ti bond in the samples.

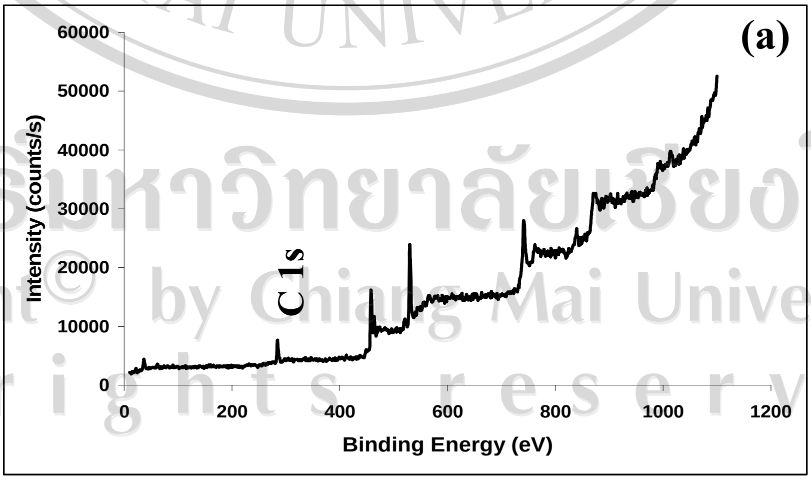

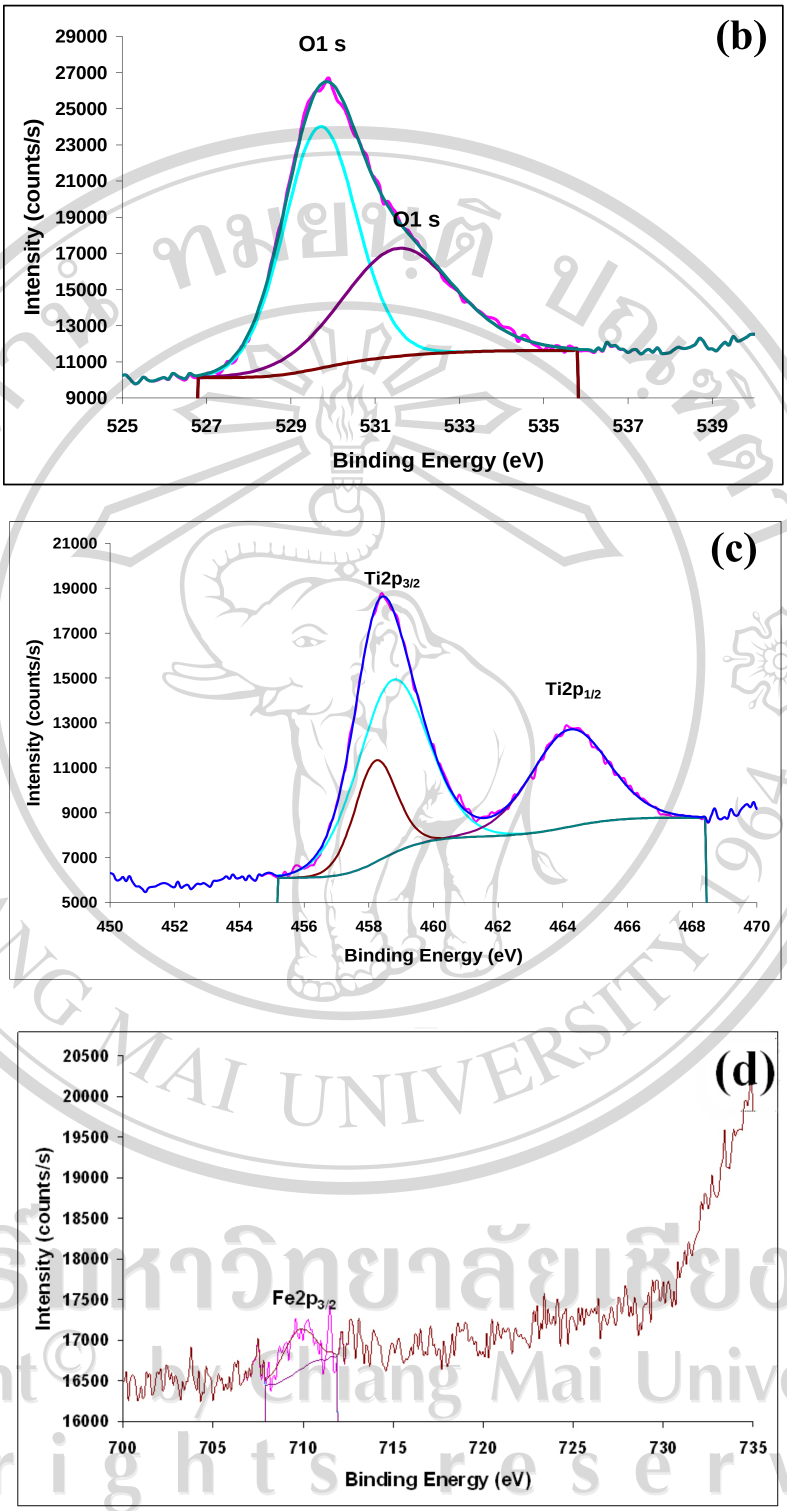

Figure 3.27 XPS spectra of 2 at.% of Fe-doped TiO_2 (a) survey, (b) Ti 2p peaks, (c) O 1s, and (d) Fe 2p peaks

3.2.6.4 XPS of 2 at.% Fe-doped TiO_2 prepared by the impregnation method

Elemental surface composition and oxidation state of elements were examined by using XPS, as shown in Figure 3.28. XPS results of the binding energy, of the most intense peaks for various samples were listed in Table 3.4. The Ti $2p_{3/2}$ and Ti $2p_{1/2}$ binding energies for 2 at.% of Fe-doped TiO_2 were found at 458.27 and 463.92. The peaks were characterized by a narrow width which indicated that the Ti existed as Ti^{4+}. Fitting of the oxygen region produced two O 1s peaks, one at about 529.53 eV and another at about 532.18 eV corresponding to O^{2-} in the TiO_2 lattice and OH^- from surface hydroxyl groups or chemisorbed water molecules, respectively. Fe-doped TiO_2 samples were characterized by the binding energy Fe $2p_{3/2}$ equal to 709.99 eV typical of Fe^{3+} [111]. The slight enhancement of Fe 2p into TiO_2 lattice indicated the formation of Fe-O-Ti bond in the samples.

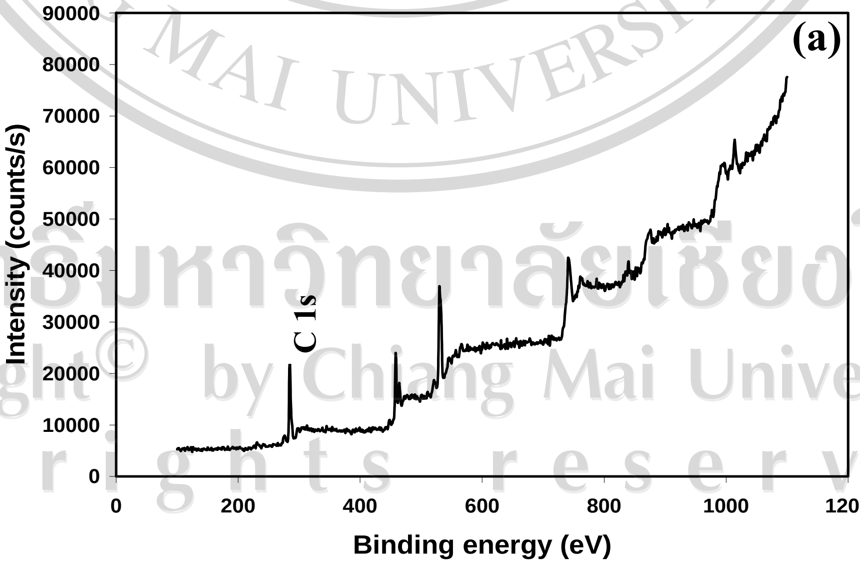

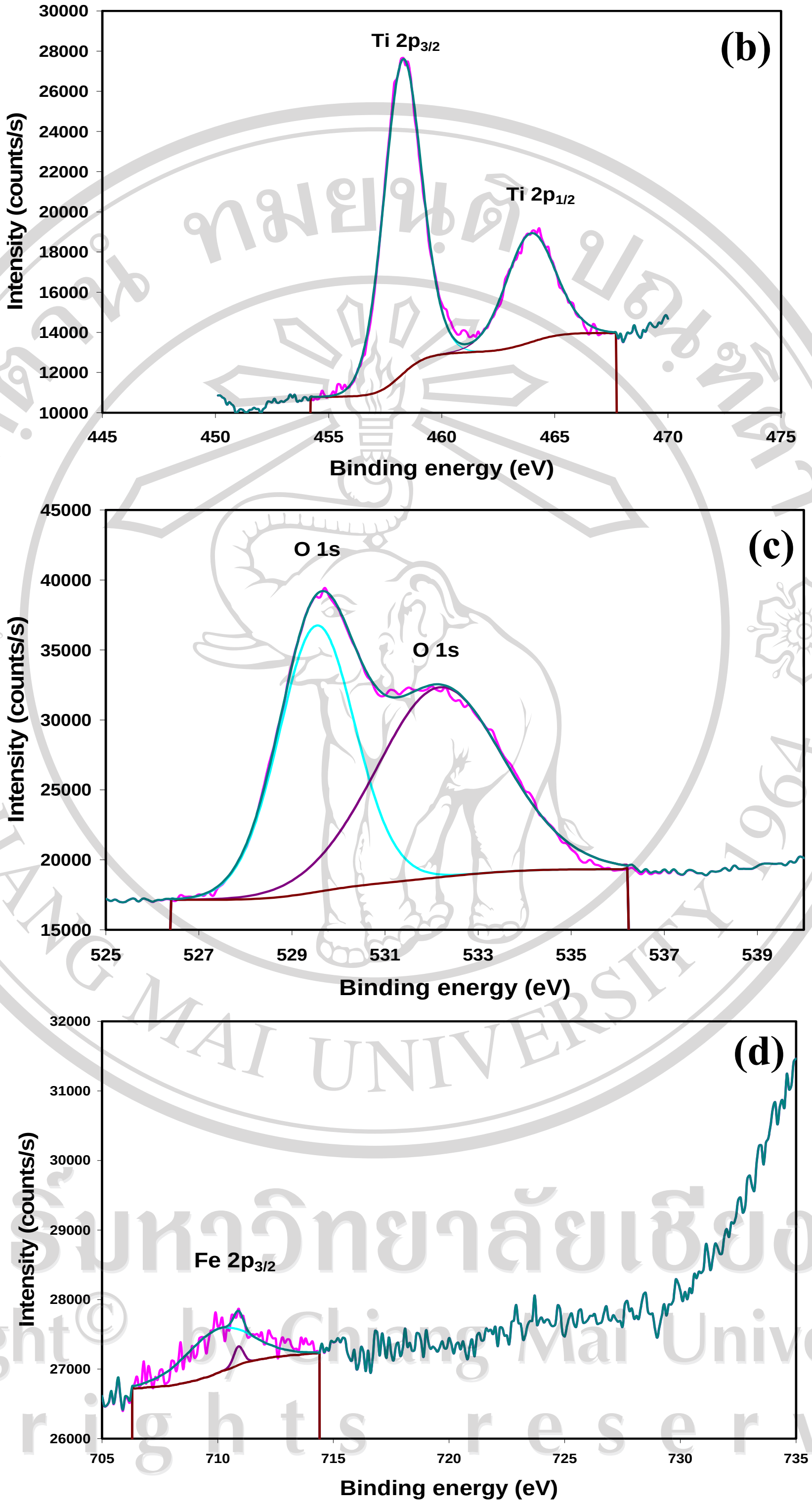

Figure 3.28 XPS spectra of pure TiO_2 and 2 at.% of Fe-doped TiO_2 prepared by impregnation method (a) survey, (b) Ti 2p peaks, (c) O 1s, and (d) Fe 2p peaks

3.3 Photocatalytic activity studies using UNSW's spiral photoreactor

3.3.1 Calibration curve

The conductivity probe was used to detect the amount of carbon generated in the spiral photoreactor. The probe was calibrated by mineralizing at different concentrations of sucrose. The calibration data from conductivity reading at different concentrations of carbon in microgram was plotted in logarithmic scale as shown in Figure 3.29 as a linear calibration curve. Table 3.5 shows the calibration data of different concentration of sucrose. Conductivity readings were converted to the mass of CO_2 generated (in terms of mass of organic carbon) by means of a calibration curve.

Table 3.5 Calibration data of different concentrations of sucrose

Amount of carbon (µg)	ln (C)	Conductivity (k, µS/cm) (initial value k=0.981)	Δk	ln (k)	ln (Δk)	Injection volume (µL)	Cumulative volume (µL)
100	4.605	2.090	1.109	0.737	0.103	20	20
400	5.991	3.780	2.799	1.330	1.029	60	80
500	6.215	4.170	3.189	1.428	1.160	20	100
800	6.685	5.180	4.199	1.645	1.434	60	160
1000	6.908	5.760	4.779	1.751	1.564	40	200
1500	7.313	7.020	6.039	1.949	1.798	100	300
2000	7.600	7.990	7.009	2.078	1.947	100	400
2500	7.824	8.920	7.939	2.188	2.072	100	500
3000	8.006	9.710	8.729	2.273	2.167	100	600
3500	8.160	10.440	9.459	2.346	2.247	100	700

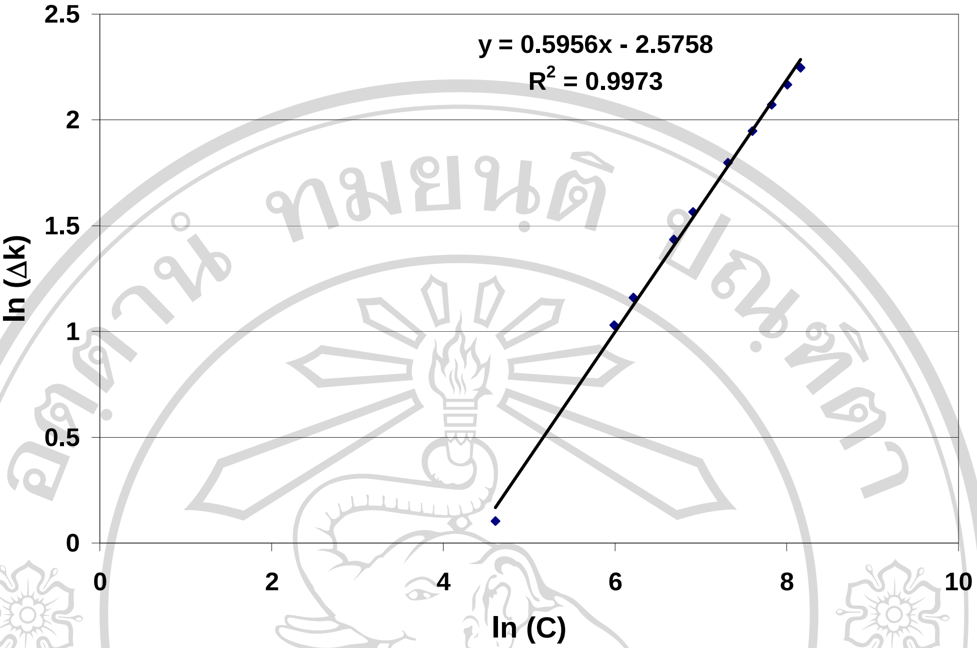

Figure 3.29 Calibration slope for conductivity probe

3.3.2 Photocatalytic activity of pure TiO_2 prepared by the modified sol-gel method

The rate of 50% mineralization of oxalic acid with 500 μg of carbon using pure TiO_2 at different calcination temperature showed the highest activity at calcination temperature of 400 °C as well as a decrease in activity at higher calcination temperature as shown in Figure 3.30. Therefore, the optimum condition of highest photoactivity mineralized oxalic acid was found at the calcination temperature 400 °C. It was found that the activity of photocatalysts decreased with high calcination temperature in the following order:

$$P25 > TiO_2\ 400\ °C > TiO_2\ 500\ °C > TiO_2\ 600\ °C > TiO_2\ 700\ °C$$

The smaller the particle size, the faster was the catalysis reaction as it directly indicated the higher specific surface area of the catalyst. To enhance the photoactivity of TiO_2, particle size, surface area, and ratio of anatase to rutile, can be controlled by changing the calcination temperature.

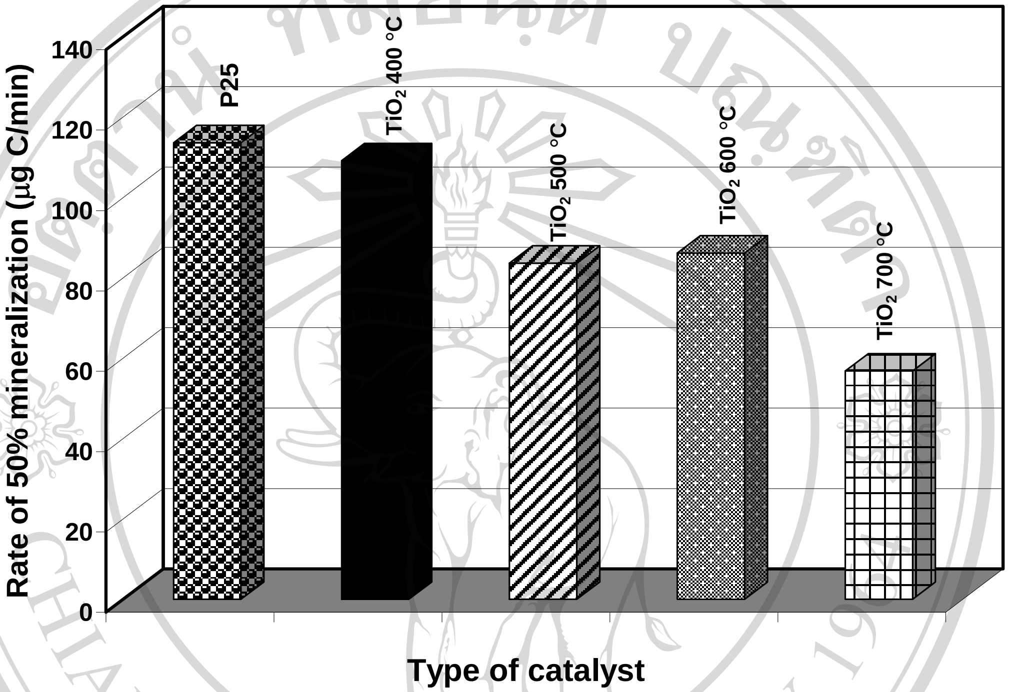

Figure 3.30 The rate of 50% mineralization rate of oxalic acid with 500 µg of carbon by Degussa P25 (as a reference) and TiO_2 at different calcination temperature 400-700 °C for 3h under UVA irradiation

3.3.3 Photocatalytic activity of V, Cu, Fe-doped TiO_2 with oxalic acid

The rate of 50% mineralization of oxalic acid with 500 µg of carbon using V, Cu, Fe-doped TiO_2 under UVA irradiation were shown in Figure 3.31-3.33. The mineralization of oxalic acid using V-doped TiO_2 indicating the highest photoactivity using 0.1 at.% of V-doped TiO_2 under UVA irradiation as shown in Figure 3.31. The mineralization of oxalic acid using Fe-doped TiO_2 increased with increasing amount of Fe (Figure 3.32). The 1 at.% of Cu-doped TiO_2 showed the highest activity mineralized oxalic acid in Figure 3.33. However, this work will be applied for water treatment under visible light, hence the optimum concentration for transition metal ions were examined with oxalic acid under visible light irradiation as shown in Figure 3.34-3.36. Therefore, the optimum condition of the highest photoactivity for V, Cu, and Fe under visible light irradiation were found to be 0.1 at.% V-doped TiO_2, 2 at.% Fe-doped TiO_2, and 0.5 at.% of Cu-doped TiO_2.

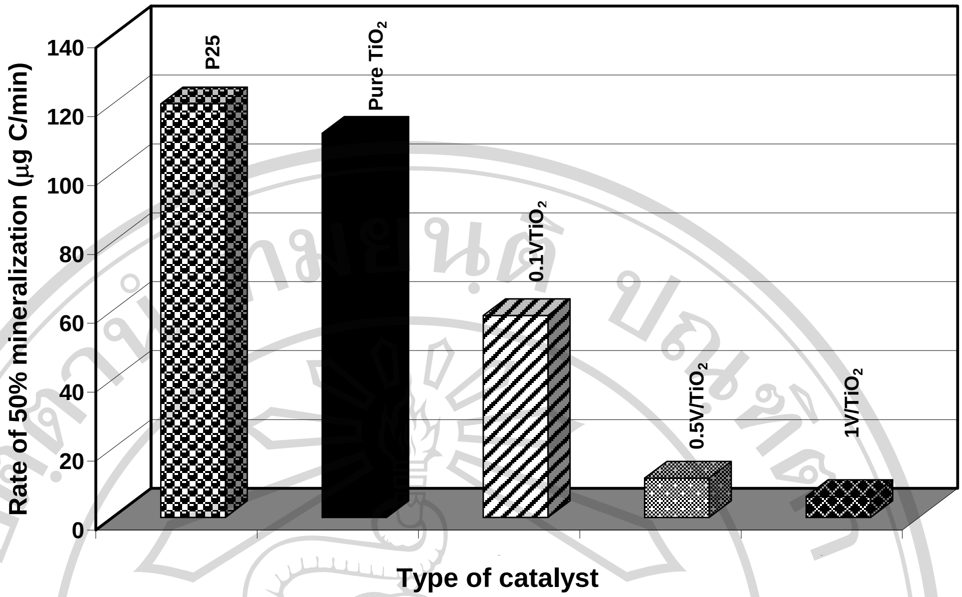

Figure 3.31 The rate of 50% mineralization of oxalic acid with 500 μg of carbon by using 0.1-1 at.% of V-doped TiO_2 under UVA irradiation

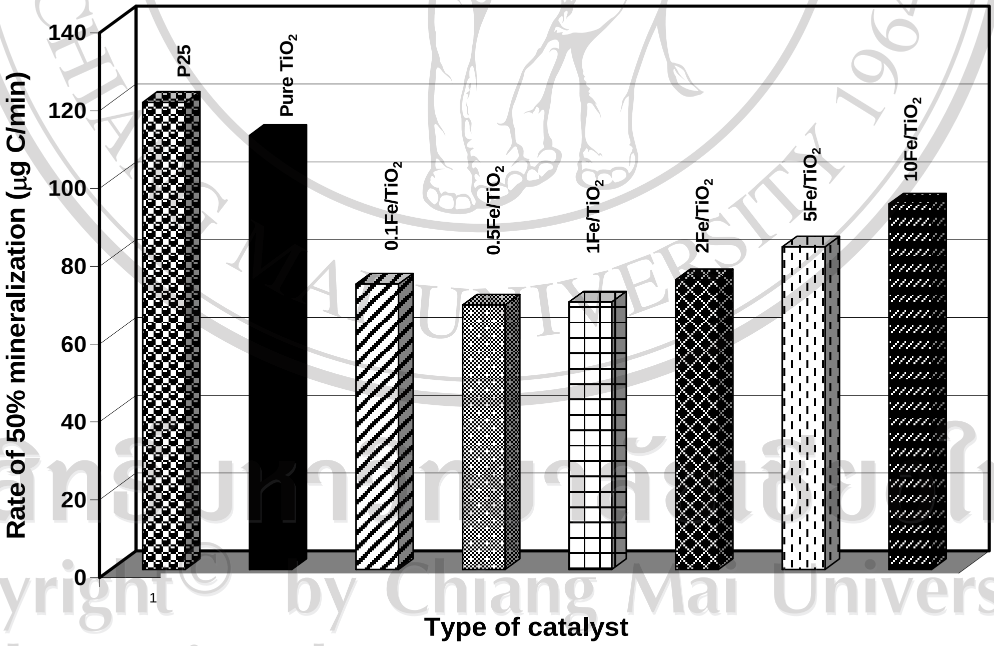

Figure 3.32 The rate of 50% mineralization of oxalic acid with 500 μg of carbon by using 0.1-10 at.% Fe-doped TiO_2 under UVA irradiation

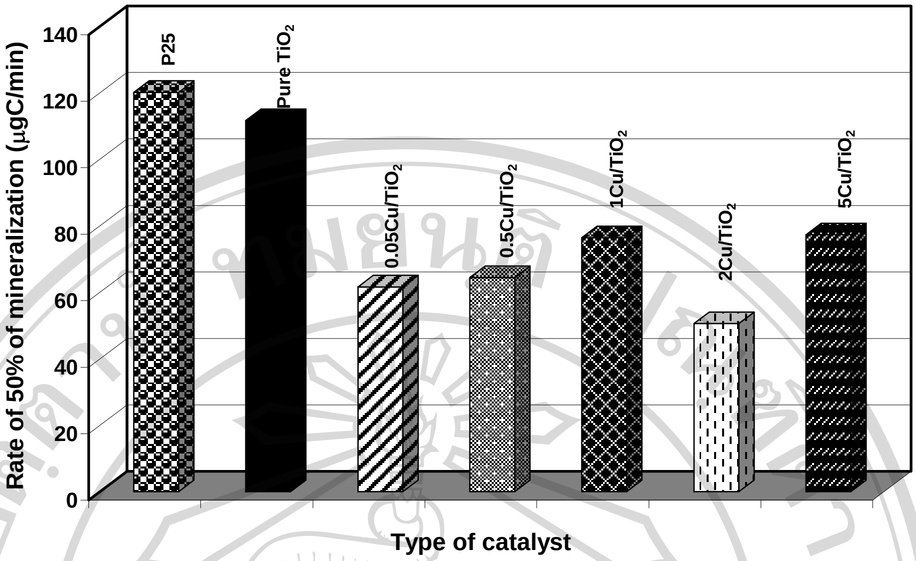

Figure 3.33 The rate of 50% mineralization of oxalic acid with 500 μg of carbon by using 0.05-5 at.% Cu-doped TiO_2 under UVA irradiation

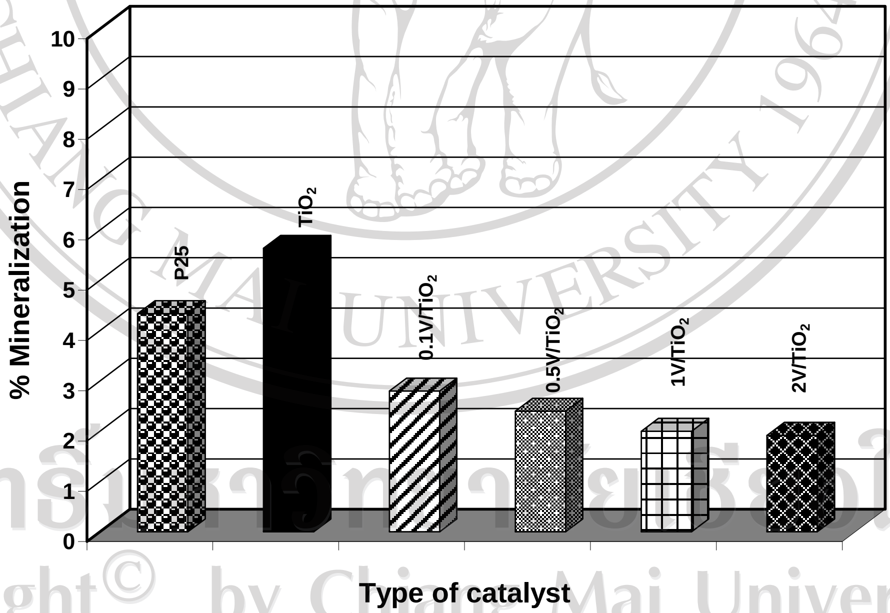

Figure 3.34 Percent mineralization of oxalic acid with 500 μg of carbon using Degussa P25, pure TiO_2, and 0.1-2 at.% of V-doped TiO_2 under visible light and irradiation time of 180 min

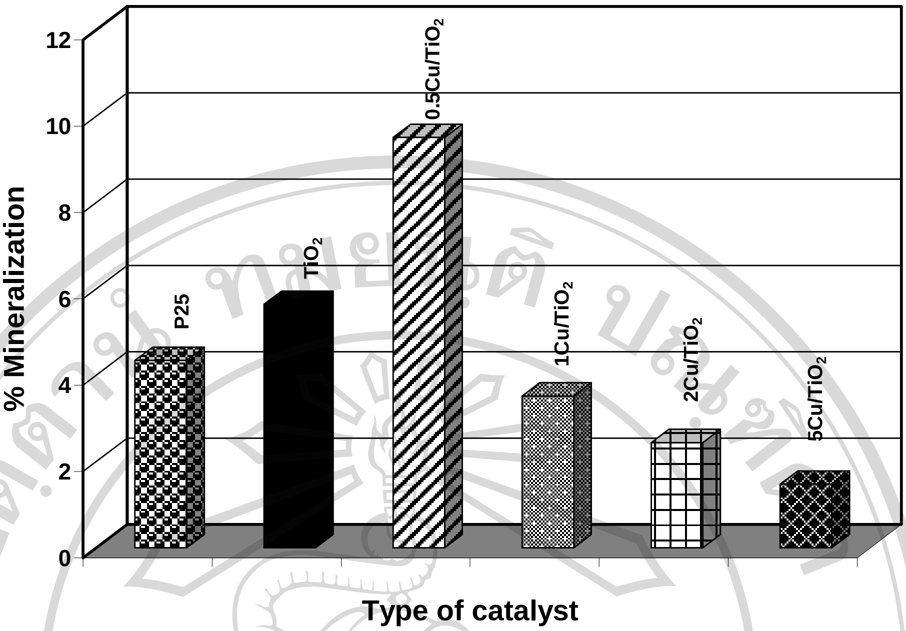

Figure 3.35 Percent mineralization of oxalic acid with 500 μg of carbon using Degussa P25, pure TiO_2, and 0.5-5 at% of Cu-doped TiO_2 under visible light and irradiation time of 180 min

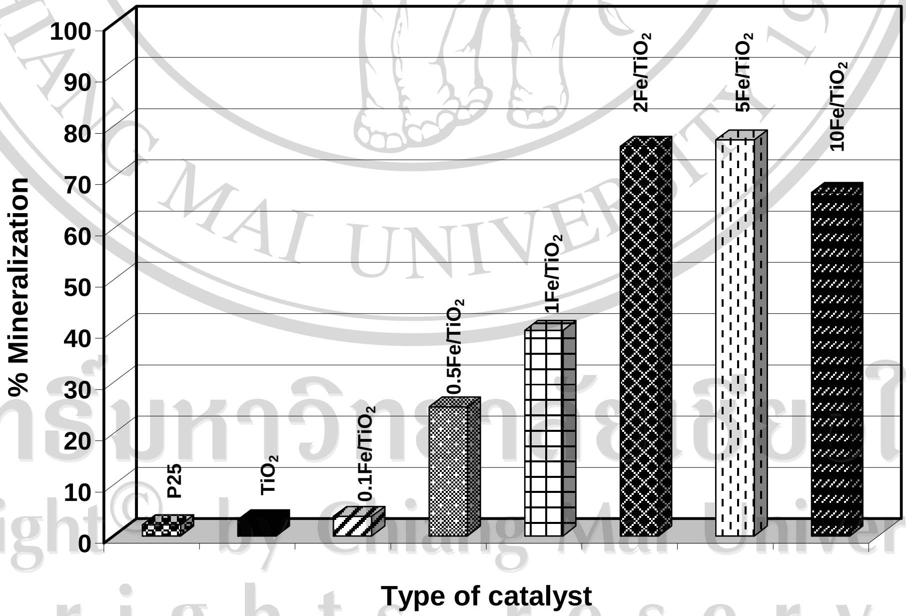

Figure 3.36 Percent mineralization of oxalic acid with 500 μg of carbon using Degussa P25, pure TiO_2, and 0.1-10 at% of Fe-doped TiO_2 under visible light and irradiation time of 90 min

3.3.4 Photocatalytic activity of V, Cu, Fe-doped TiO_2 with various organic compounds under UVA, solar light, and visible light irradiation

The efficiency of mineralization was studied in organic compounds: sucrose, phenol, formic acid, oxalic acid, methanol and malonic acid under near UV, solar light, and visible light irradiation. The mineralization rate of different organic compounds was compared for various photocatalysts under UVA irradiation (Figure 3.37). It could be seen that Degussa P25 was the most active photocatalyst for mineralizing of all organic compounds under UVA irradiation. It was found that overall the activity of the photocatalysts decreased in the following order:

P25 > pure TiO_2 > Cu-doped TiO_2 > Fe-doped TiO_2 > V-doped TiO_2

Fe-doped TiO_2 significantly outperformed Cu-doped TiO_2 only in mineralizing oxalic acid.

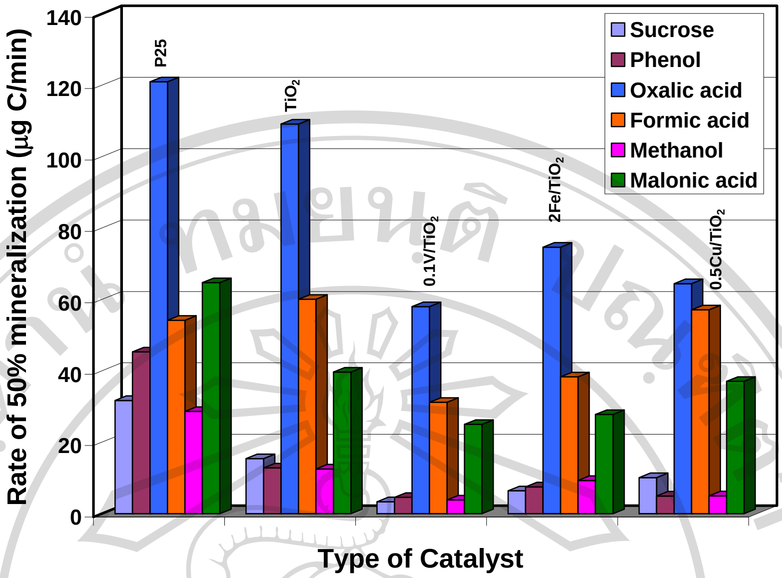

Figure 3.37 The rate of 50% mineralization of sucrose, phenol, oxalic acid, formic acid, methanol, and malonic acid with 500 µg of carbon by various photocatalysts under UVA irradiation

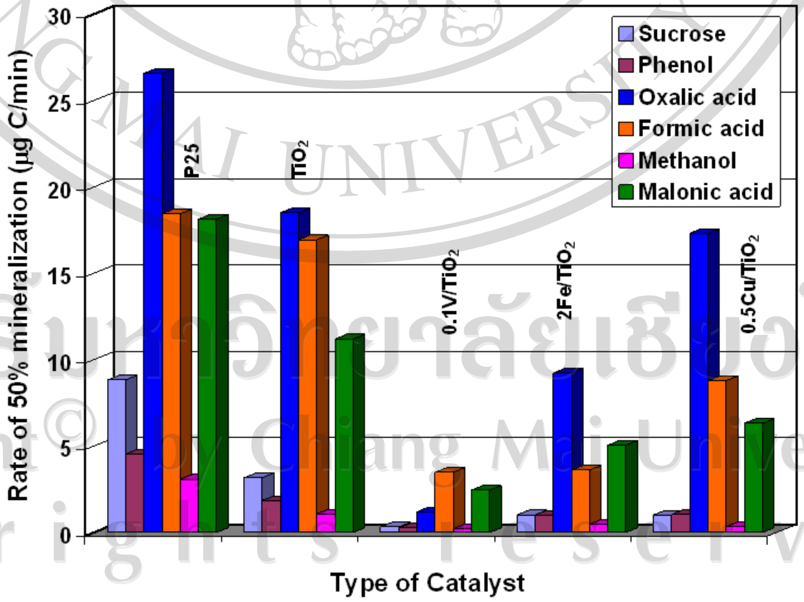

Figure 3.38 The rate of 50% mineralization of sucrose, phenol, oxalic acid, formic acid, methanol, and malonic acid with 500 µg of carbon by using various photocatalysts under solar light irradiation

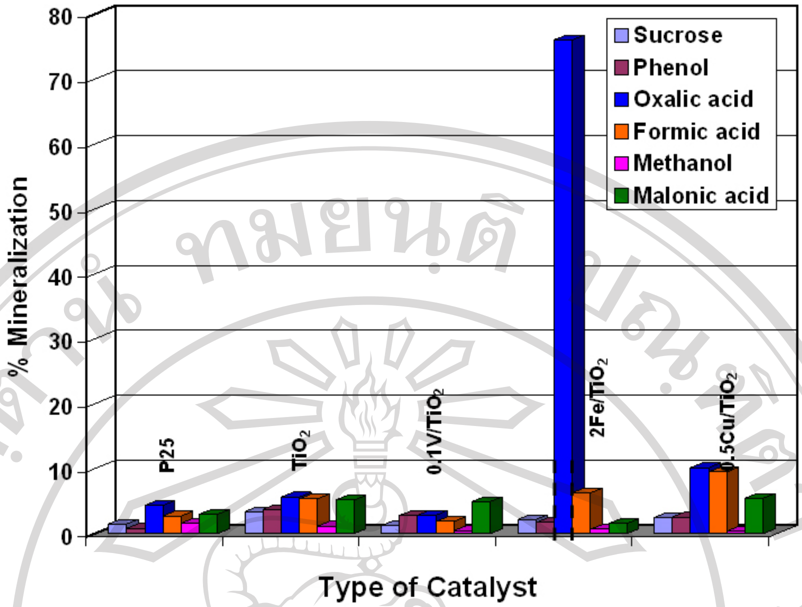

Figure 3.39 Mineralization of sucrose, phenol, oxalic acid, formic acid, methanol, and malonic acid with 500 μg of carbon by using various photocatalytsts under visible light illumination (fixed irradiation time = 3h, except 2 at.% of Fe doped TiO_2 fixed irradiation time = 90 min for oxalic acid)

The 50% mineralization rates of a range of organic compounds using various photocatalysts under solar spectrum irradiation were compared in Figure 3.38. It was also found that Degussa P25 and pure TiO_2 were more active than any doped TiO_2. Cu-doped TiO_2 performed better than Fe-doped TiO_2 under the solar spectrum illumination, even in the mineralization of oxalic acid. Vanadium ion was found to be the most detrimental dopant in mineralizing all organic compounds. This could be explained by the significant change in the absorption properties of the V-doped TiO_2 as shown in Figure 3.1. The TiO_2 doping with Cu has the least shift in the absorption properties (Figure 3.2), therefore has the least detrimental effects under UVA and solar spectrum illumination. Addition of Fe^{3+} resulted in a dramatic increase in the photocurrent, higher than in the case of Cu^{2+} as reviewed by Litter (1999) [99]. The greater efficiency of Fe^{3+} may be due to the ability of Fe^{2+} to migrate away from the particle into solution, preventing the deleterious back-reaction; in contrast, Cu^0 was immobilized on the particle.

Litter (1999) [99] referred to Okamoto's research on the effect of addition of Cu^{2+} in the photocatalytic decomposition of phenol over anatase powder that Cu^{2+} acted positively or negatively, depending on the concentration. Cu^{2+} increased the photoactivity rate but a larger amount of Cu was detrimental. Moreover, Cu^{2+} showed a negative effect at all concentrations, attributed to the fact that the short-circuiting of the cupric ion (reactions (3.2) and (3.3)) were very severe.

$$\mathrm{Cu^{2+}} \xrightarrow{e^-} \mathrm{Cu^+} \xrightarrow{e^-} \mathrm{Cu} \tag{3.2}$$

$$\mathrm{Cu} \xrightarrow{h^+} \mathrm{Cu^+} \xrightarrow{h^+} \mathrm{Cu^{2+}} \tag{3.3}$$

Many researchers [99, 114, 119] proposed that metal cations can increase the oxidation rate by participating not only in heterogeneous pathways but also in alternative Fenton-type reactions that produced additional $OH^\bullet$ according to reaction (3.4). It could be possible that the enhancement photocatalytic activity of Fe, Cu-doped TiO_2 with oxalic acid and formic acid under visible light irradiation were due to the formation of complex. The complexation of Fe, Cu-doped TiO_2 with oxalic acid and formic acid were investigated and discussed in the next part with FT-IR results.

$$\mathrm{M}^{(n-1)+} + \mathrm{H_2O_2} + \mathrm{H^+} \longrightarrow \mathrm{M}^{n+} + \mathrm{OH}^\bullet + \mathrm{OH}^- \tag{3.4}$$

The trapping of electrons by Cu^{2+} and the trapping of holes by its reduced form were proposed to explain the decrease of the e^-/h^+ recombination rate and a higher production of $HO^{\bullet}$ radicals [99]. An alternative explanation was based on the effect of Cu^+ as a catalyst for the Fenton reaction (reaction (3.5)):

$$Cu^{+} + H_2O_2 \rightarrow Cu^{2+} + OH^{\bullet} + OH^{-} \qquad (3.5)$$

The reduction rate of mineralization organic compounds followed Okamoto's report explaining that the negative effect of high Cu^{2+} concentrations was attributed to the short circuiting reactions that created a cyclic process without generating active $HO^{\bullet}$ radicals and retarded the reaction.

An excess of iron ion was detrimental due to the short-circuiting reactions (3.6) and (3.7), as proposed by Fujihira et al. in Litter's review (1999) [99]. If H_2O_2 was added to the system, both ferric and cupric ions remarkably enhanced the rate, even at high concentrations. The effect was explained by the role of metal ions as catalysts in decomposing H_2O_2 through photo-Fenton reaction.

$$Fe^{3+} + e^{-} \rightarrow Fe^{2+} \qquad (3.6)$$

$$Fe^{2+} + h^{+} \rightarrow Fe^{3+} \qquad (3.7)$$

Under visible light irradiation, Fe-doped TiO_2 (at its optimum doping of 2 at.%) outperformed other photocatalysts in mineralizing oxalic acid (Figure 3.36). Using 2 at.% of Fe-TiO_2 for mineralizing oxalic acid should be considered more favourably due to lower doping iron compared to 5 at% Fe-TiO_2. All Fe-TiO_2 displayed higher photoactivity than neat TiO_2 in mineralizing oxalic acid under visible light illumination. When the dopant concentration was too high, the recombination rate of electron and hole would increase because band gap energy decreased and competed with the redox processes because the distance between trapping sites of electrons and holes was decreased. After 90 min of visible light irradiation, the mineralization of oxalic acid of 2, 5, 10 at.% of Fe-doped TiO_2 approached plateau and not be able to complete mineralization. The light source was switched to UV-illumination for the completion of mineralization. Mineralization of oxalic acid increased with illumination time under visible light irradiation. Samples of 0.1, 0.5, 1 at.% of Fe-doped TiO_2 to mineralize oxalic acid were considered to be too slow. The performances of all samples were compared with the mineralization of oxalic acid at 90 min with visible light. The system was subjected to with a second stage of UV irradiation in order to completely mineralize the organic fraction in the system. The decrease of the photoactivity of 2 at.% V-doped TiO_2, 5 at% Cu-doped TiO_2, and 10 at.% Fe-doped TiO_2 could be explained that the dopants act more as recombination centers than as trap sites for charge transfer at the interface. Doping TiO_2 with various transition metal ions may lead to an enhanced efficiency of the photocatalytic systems. The dominant parameters include the character and concentration of dopants and the applied thermal treatment. The total induced alteration of the photocatalytic activity made up from the sum of changes which occur in: (i) the light-absorption capability of the TiO_2 photocatalyst, (ii) adsorption capacity of the substrate molecules at the catalyst's surface and (iii) interfacial charge transfer rate

Many controversial results were reported in literatures since the method of doping leads to different morphological and crystalline properties of the photocatalyst. Impregnation and sol–gel methods were used for metal ions doping into TiO_2. As the concentration of the dopant increases, the band gap energy becomes narrower, the electron–hole pairs within the region are efficiently separated before recombination. Moreover, when the band gap energy becomes very narrow the penetration depth of light into TiO_2 greatly exceeds the band gap layer. The low photoactivity occurrs as a result of the recombination of electron-hole. The recombination of photogenerated electron–hole pairs in the TiO_2 semiconductor increase because there is no suitable energy to separate them. Due to the fact that doping ions act as trapping sites, they can influence the lifetime of charge carriers. Usually, they enhance the recombination of photogenerated electrons and holes, and therefore do not allow reactions to proceed with any noticeable effect under either under ultraviolet or visible light. Fe^{3+} ion has a half-filled electronic configuration (d^5) that is known to be stable. When the Fe^{3+} ion traps electrons, the half-filled electronic configuration is destroyed and their stability decreases. The trapped electrons can easily be transferred to oxygen adsorbed on the surface of the catalyst and the Fe^{3+} ion return to the original stable half-filled electron structure. This might promote charge transfer and efficient separation of the electrons and holes by trapped electrons. The prerequisite for an effective dopant involves the possibility of charge detrapping and migration to the surface. The reasons for special attention of iron-doped TiO_2 are as follows: (i) iron cations have a large influence on the charge-carrier recombination time, (ii) the use of iron-doped photocatalyst is efficient in several important photocatalytical reduction and oxidation reactions. Iron cations occupy substitutional positions because of the similar radius of Fe^{3+} and Ti^{4+} and form solid solutions with titania at low concentrations and the existence of solubility limits for

Fe ions in TiO_2 lead to formation of iron oxide at higher concentrations. Araña et al. (2004) [110] discussed the oxidation of oligocarboxylic acids and a mechanism via a [Fe–carboxylic acid]$^{n+}$ complex was proposed. Complexes formed by iron interaction with formic and maleic acids are more photoactive than those formed with acetic or acrylic acids. The slower degradation of these last two acids could be related to a photo-Kolbe reaction or other reduction processes. Impregnation of TiO_2 Degussa with iron nitrate was found to be effective for oxalic and EDTA degradation but less active for maleic acid oxidation [112].

3.4 Photocatalytic activity studies using CMU's spiral photoreactor

3.4.1 Calibration curve

The conductivity probe was used to detect the amount of carbon generated in the spiral reactor. The probe was calibrated by mineralizing at different concentrations of sucrose. The calibration data from conductivity reading at different concentrations of carbon in microgram was plotted in logarithmic scale as shown in the Figure 3.40 as a linear calibration curve. Table 3.6 shows the calibration data of different concentrations of sucrose. Conductivity readings were converted to the mass of CO_2 generated (in terms of mass of organic carbon) by means of a calibration curve.

Table 3.6 Calibration data of different concentrations of sucrose

Amount of carbon (μg)	ln (C)	Conductivity (k, μS/cm) (initial value k=2.57)	Δk	ln (k)	ln (Δk)	Injetion volume (μL)	Cumulative volume (μL)
100	4.6051	2.72	0.15	1.0006	-1.8971	20	20
400	5.7037	3.19	0.62	1.1600	-0.4780	60	80
500	6.2146	3.55	0.98	1.2669	-0.0202	20	100
700	6.5510	3.87	1.3	1.3532	0.2623	40	140
1000	6.9077	4.21	1.64	1.4374	0.4946	60	200

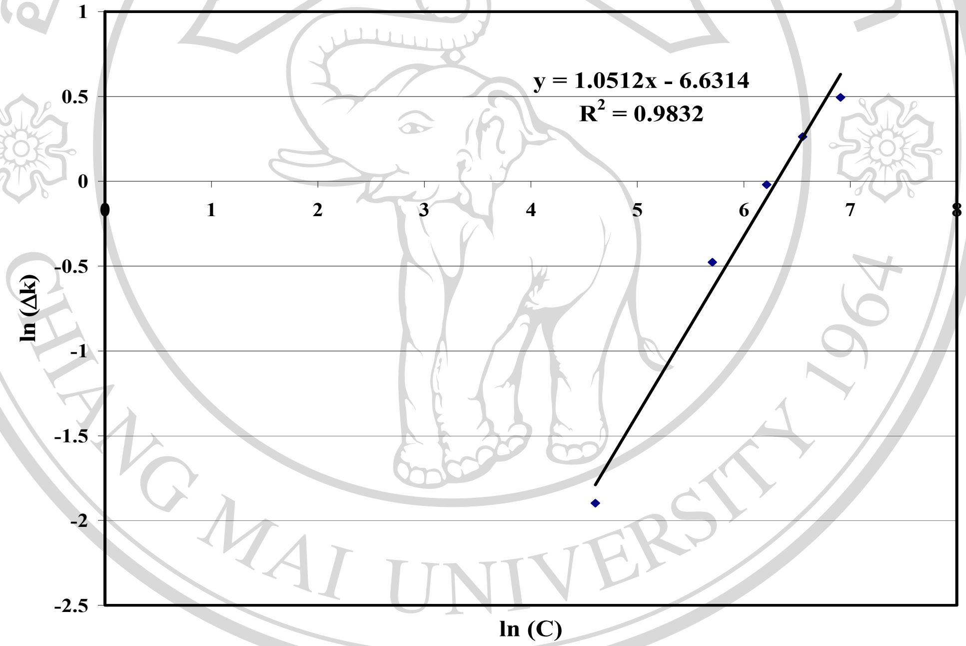

Figure 3.40 Calibration slope for conductivity probe

3.4.2 Photocatalytic activity of Fe-doped TiO_2 prepared by the impregnation method

3.4.2.1 Photocatalytic activity of Fe-doped TiO_2 with oxalic acid under UVA, solar light, and visible light irradiation

Fe-doped TiO_2 was successfully prepared by the impregnation method. The impregnation method has many advantages such as the actual amount of doping iron on TiO_2 could be prepared and was easy for preparing the doped catalysts. When doping with iron the same amount of Fe dopant, it could be seen the different color of the powder obtained by the impregnation method and the modified sol-gel method. The color of Fe-doped TiO_2 prepared by the impregnation method was dark reddish color, while Fe-doped TiO_2 prepared by the modified sol-gel method was less reddish at the same amount of iron.

The highest photoactivity of mineralization oxalic acid of Fe-doped TiO_2 was found by using 1 at.% of Fe-doped TiO_2 under UVA irradiation but under solar light irradiation, the highest photoactivity of mineralized oxalic acid was found to be 2 at.% of Fe-doped TiO_2 as shown in Figures 3.41-3.43. The optimum concentration for Fe-doped TiO_2 was examined with oxalic acid under visible light irradiation as shown in Figure 3.43 as 2 at.% Fe-doped TiO_2.

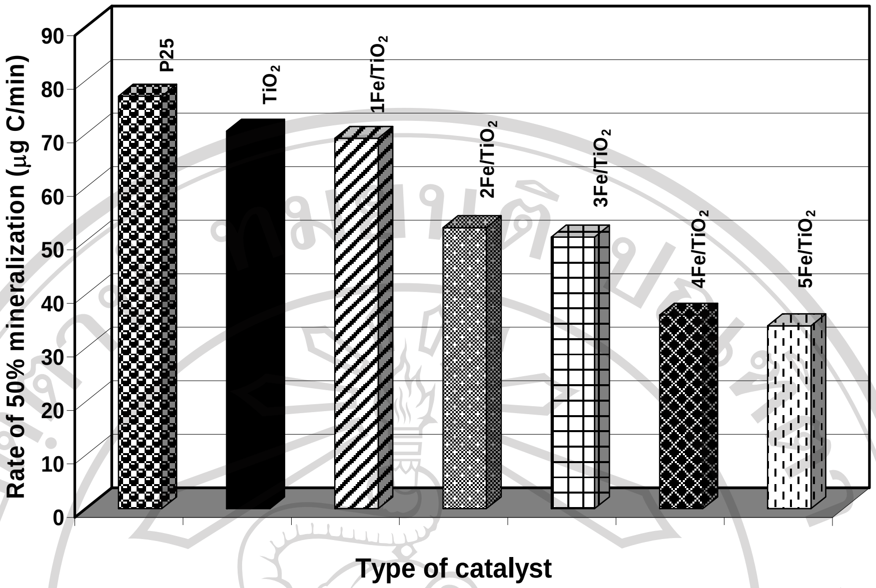

Figure 3.41 The rate of 50% mineralization of oxalic acid with 500 µg of carbon by using 1-5 at.% of Fe-doped TiO_2 under UVA irradiation as compare to P25 and pure TiO_2

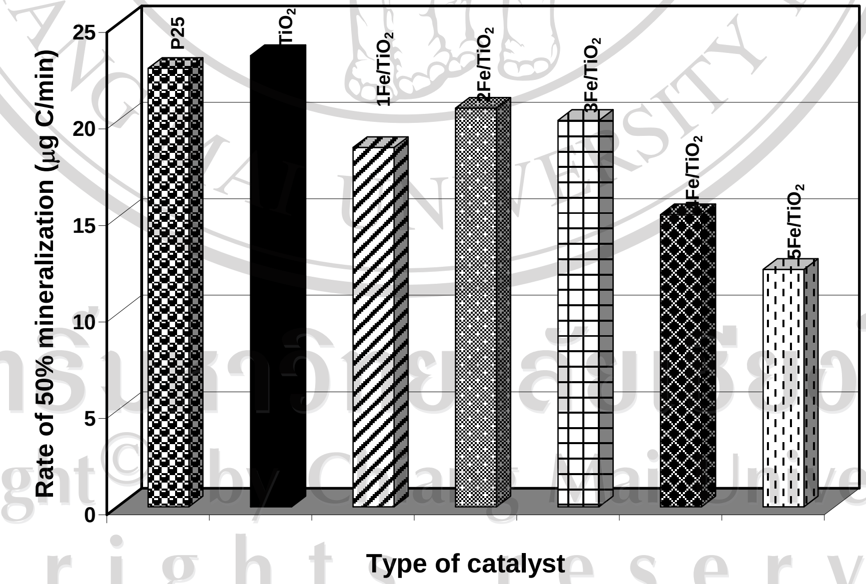

Figure 3.42 The rate of 50% mineralization of oxalic acid with 500 µg of carbon by using 1-5 at.% of Fe-doped TiO_2 under solar light irradiation as compare to P25 and pure TiO_2

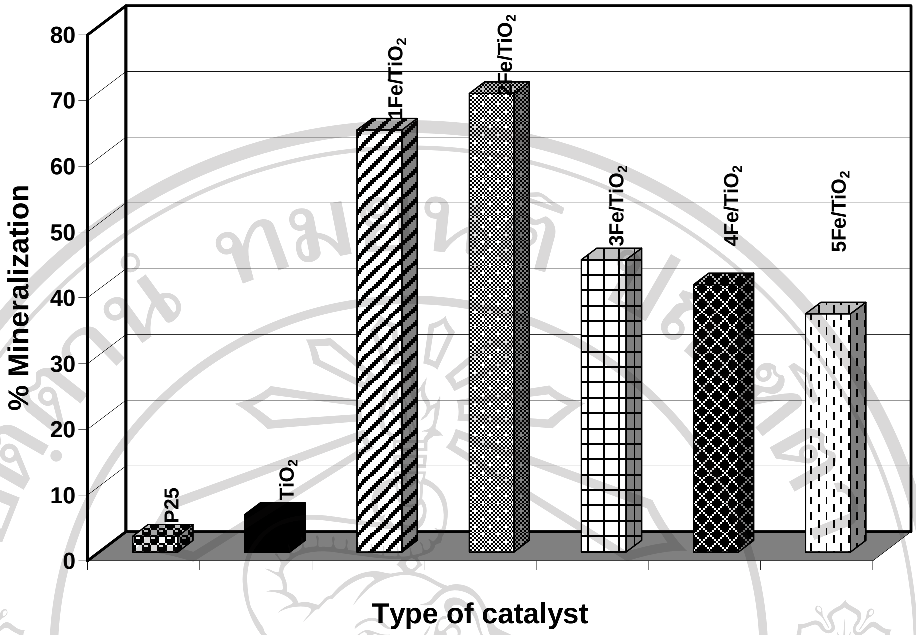

Figure 3.43 Mineralization of oxalic acid with 500 µg of carbon by using 1-5 at.% of Fe doping under visible light illumination fixed irradiation time = 50 min as compared to P25 and TiO_2

3.4.2.2 Photocatalytic activity of Fe-doped TiO_2 with various organic compounds under UVA, solar light, and visible light irradiation

The efficiency of mineralization was studied in organic compounds as: sucrose, phenol, formic acid, oxalic acid, and methanol under near UVA, solar light, and visible light irradiation. Figure 3.44 shows the comparison of the 50% mineralization rate of different organic compounds for various photocatalysts under UVA irradiation. It could be seen that Degussa P25 was the most active photocatalyst for mineralizing of all organic compounds under UVA irradiation. The overall the activity of the photocatalysts decreased in the following order:

P25 > pure TiO_2 > Fe-doped TiO_2

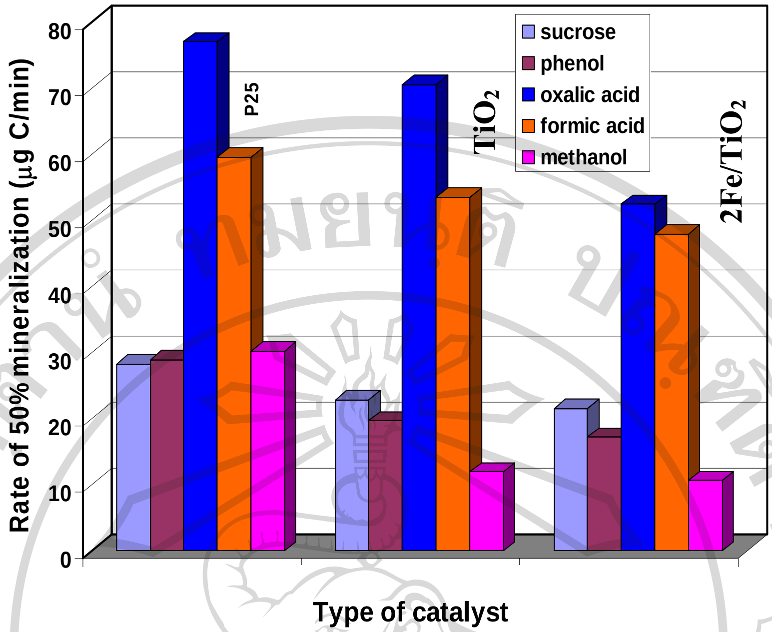

Figure 3.44 The rate of 50% mineralization of sucrose, phenol, oxalic acid, formic acid, and methanol with 500 µg of carbon by using various photocatalysts under UVA irradiation

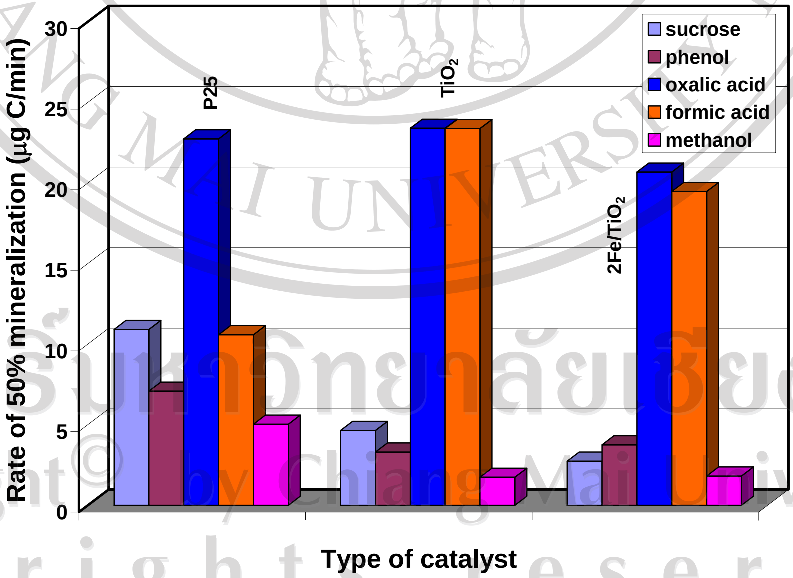

Figure 3.45 The rate of 50% mineralization of sucrose, phenol, oxalic acid, formic acid, and methanol with 500 µg of carbon by using various photocatalysts under solar light irradiation

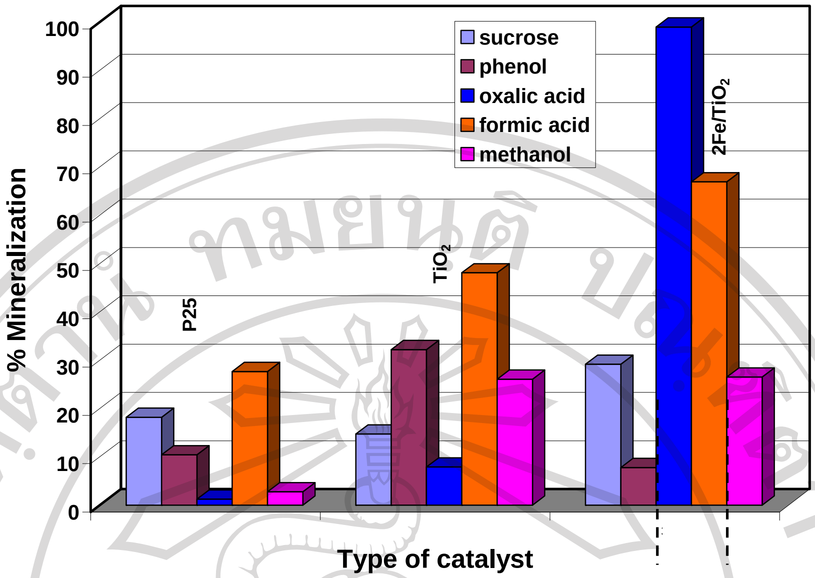

Figure 3.46 Mineralization of sucrose, phenol, oxalic acid, formic acid, and methanol with 500 µg of carbon by using various photocatalytsts under visible light illumination (fixed irradiation time = 3h, except 2 at.% of Fe-doped TiO_2 fixed irradiation time = 50 min for oxalic acid)

The 50% mineralization rates of a range of organic compounds using various photocatalysts under solar spectrum irradiation were compared. It was also found that pure TiO_2 was more active than Degussa P25 and Fe-doped TiO_2 when mineralized oxalic acid and formic acid as shown in Figure 3.45.

Under visible light irradiation, Fe-doped TiO_2 prepared by the impregnation method (at its optimum doping of 2 at.%) outperformed other photocatalysts in mineralizing oxalic acid and formic acid as shown in Figure 3.46. All Fe-doped TiO_2 displayed higher photoactivity than neat TiO_2 in mineralizing only oxalic acid under visible light illumination as shown in Figure 3.46. When the dopant concentration is too high, the recombination rate of electron and hole will increase because the decrease in the band gap energy and compete with the redox processes because the decrease in the distance between trapping sites of electrons and holes. After 50 min of visible light irradiation, the mineralization of oxalic acid of 1-5 at.% of Fe-doped TiO_2 approached plateau and not be able to complete mineralization. The light source was switched to UV-illumination for the completion of mineralization. Mineralization of oxalic acid increased with illumination time under visible light irradiation. Samples of 3, 4, 5 at.% of Fe-doped TiO_2 mineralized oxalic acid were considered to be too slow. The system was subjected to a second stage of UV irradiation in order to completely mineralize the organic fraction in the system. The Fe-doped TiO_2 photocatalysts prepared by the modified sol-gel method and impregnation method could be more efficient than Degussa P25 and pure TiO_2 under visible light irradiation mainly if the following considerations can be accomplished, (i) the recombination rate was decreased by the presence of iron ion acting as electron or hole traps, (ii) no separated phases of iron oxide or mixed oxides such as hematile or pseudobrookite which are less active than TiO_2. Direct oxidation of formic acid was expected to be a low efficient process because it caused the formation of a highly unstable $H^{\bullet}$ radical in solution as mentioned in Franch's reported [112].

3.5 Fourier transform infrared spectrophotometry studies

The enhanced performance was observed for the Fe-doped TiO_2 system likely due to the formation of ferric-oxalate complex that could generate hydroxyl radical. The interaction between Fe^{3+}-oxalate and the possibility of Fe^{3+}-oxalate complexation were studied by using FT-IR analysis. The characteristic infrared bands of oxalic acid and formic acid as mentioned in the literatures as shown in Table 3.7. FT-IR spectra of pure TiO_2, Fe, Cu-doped TiO_2, and Fe, Cu-doped TiO_2 with oxalic acid and formic acid were compared as shown in Figure 3.47-3.49. Spectrum of pure TiO_2 showed broad band centered at 3500-3150 cm^{-1}, ascribed to basic hydroxyl groups, whereas the bands of O-H bending at 1630 cm^{-1}, N-H bending at 1400 cm^{-1}, and Ti-O stretching at 700-500 cm^{-1} correspond to adsorbed molecular water, ammonia, and Ti interacted with oxygen, respectively. Figure 3.47 and 3.48 shows the FT-IR spectra from 2 at.% Fe-doped TiO_2 prepared by the modified sol-gel method and the impregnation method with oxalic acid interaction after 15 min of visible light illumination respectively. The broad peak between 3500-3150 cm^{-1} represented surface H-bounded hydroxyl groups as shown in Figure 3.47-3.48 (a), (b), (c), (d), (e), (f). Two other peaks of adsorbed oxalate were also found at ~1700 cm^{-1} for C=O stretching and at ~1300 cm^{-1} for C-O stretching as shown in Figure 3.47(d) and 3.48(d). The characteristic FT-IR peaks of adsorbed oxalate were found in the Hug's report [116], the two prominent peaks of adsorbed oxalate at 1715-1713 and 1696-1679 cm^{-1} was symmetric and asymmetric combinations of two C=O double bonds (ν_sC=O and ν_{as}C=O), respectively. Two other strong peaks was at 1424-1412 cm^{-1} (ν_sC-O+(ν_sC-C) and at 1279-1264 cm^{-1}(ν_{as}C-O+ν_{as}C-C). The peaks of 2 at.% Fe-doped TiO_2 with adsorbed oxalic acid at 1700 and 1300 cm^{-1} had higher intensity than those in bare Fe-doped TiO_2. The spectra of adsorbed oxalate ions obtained from this study indicated that oxalate ions formed strong surface complexes on Fe-doped TiO_2 surface. Similarly, several literatures reported that Fe-oxalate complex could strongly absorbed at low pH conditions [41, 108, 113].

The interaction of between Fe^{3+}-formate and the possibility of Fe^{3+}-formate complexation were studied by using FT-IR analysis. Figure 3.47 and 3.48 shows the spectra from 2 at.% Fe-doped TiO_2 prepared by the modified sol-gel method and the impregnation method with formic acid interaction after 15 min of visible light illumination. The broad peak between 3500-3150 cm^{-1} represented surface H-bounded hydroxyl groups as shown in Figure 3.47 and 3.49 (a), (b), (c), (d), (e), (f). The Fe^{3+}-formate interaction could show the characteristic vibrations at ~1600 for C=O stretching and at ~1300 cm^{-1} for C–O stretching. The Fe^{3+}-formate was found at higher wavenumbers at ~1300 cm^{-1} (Figure 3.47(c) and 3.48(c)). Fe^{3+}-formate complexes was described in the literature showing ν_{as}(HCOO-) and ν_s(HCOO-) vibrations at 1590 and 1370 cm^{-1}[117].

Figure 3.49 (c) and (d) shows oxalic acid and formic acid molecule interacted with Cu-doped TiO_2 under visible light irradiation for 15 min. The broad peak between 3500-3000 cm^{-1} was indicated H-bounded hydroxyl groups as shown in Figure 3.49 (a), (b), (c), (d), (e), (f). Two other peaks of adsorbed oxalate were also found C=O stretching at ~1700 cm^{-1} and C-O stretching at ~1300 cm^{-1}. The peaks of 0.5 at.% Cu-doped TiO_2 with adsorbed oxalic acid at 1700 and 1300 cm^{-1} had higher intensity than those in bare Cu-doped TiO_2 as shown in Figure 3.49(c). The spectra of adsorbed oxalate ions obtained from this study indicated that oxalate ions form strong surface complexes on Cu-doped TiO_2 surface. The Cu^{2+}-formate interaction could show the characteristic vibrations of C=O stretching at ~1600 cm^{-1} and C–O stretching at ~1300 cm^{-1}. The Cu^{2+}-formate has a strong band in the region around 1300 cm^{-1} as also shown in Figure 3.49(b). The peaks of 0.5 at.% Cu-doped TiO_2 interacted with formic acid were higher than the bare Cu-doped TiO_2.

Axe et al. (2006) [115] studied competitive adsorption of oxalate ions at water-goethite interface. The results of oxalate ions adsorbed on goethite interface revealed that the peak area varied as a function of pH, and the stronger oxalate ions adsorption. Hug and Bahnemann (2006) [116] reported that oxalate ion was the only one of the three dicarboxylates that formed additional surface complexes at low pHs. The surface species formed at low pHs could either be protonated, adsorbed or strongly hydrogen-bounded with a neighboring protonated hydroxyl group.

Table 3.7 FT-IR absorption bands of oxalic acid and formic acid [114-118]

Oxalic acid	
Wavenumber (cm^{-1})	Assignment
3000-2500	O-H, stretch, very broad
2700-2500	Overtones and combinations
1740-1680	C=O, stretch, strong
1440-1395	C-O-H in plane bending
1315-1280	C-O, stretch, strong
960-875	C-O-H out of plane bending
Formic acid	
3000-2500	O-H, stretch
1724-1722	C=O, stretch
1214-1185	C-O, stretch
1160	CO–OH

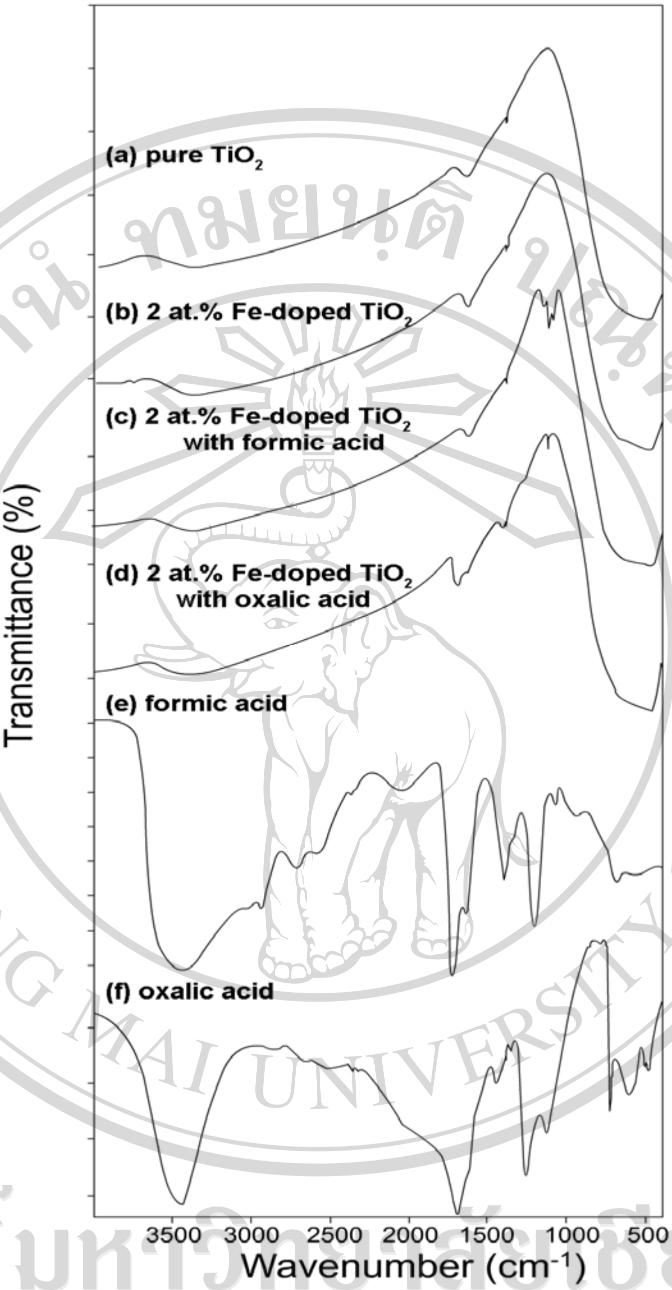

Figure 3.47 FT-IR spectra of (a) pure TiO_2, (b) 2 at.% of Fe-doped TiO_2 (the modified sol-gel method, (c) 2 at.% of Fe-doped TiO_2 with formic acid, (d) 2 at.% of Fe-doped TiO_2 with oxalic acid after mineralization under visible light for 15 min, (e) formic acid, and (f) oxalic acid

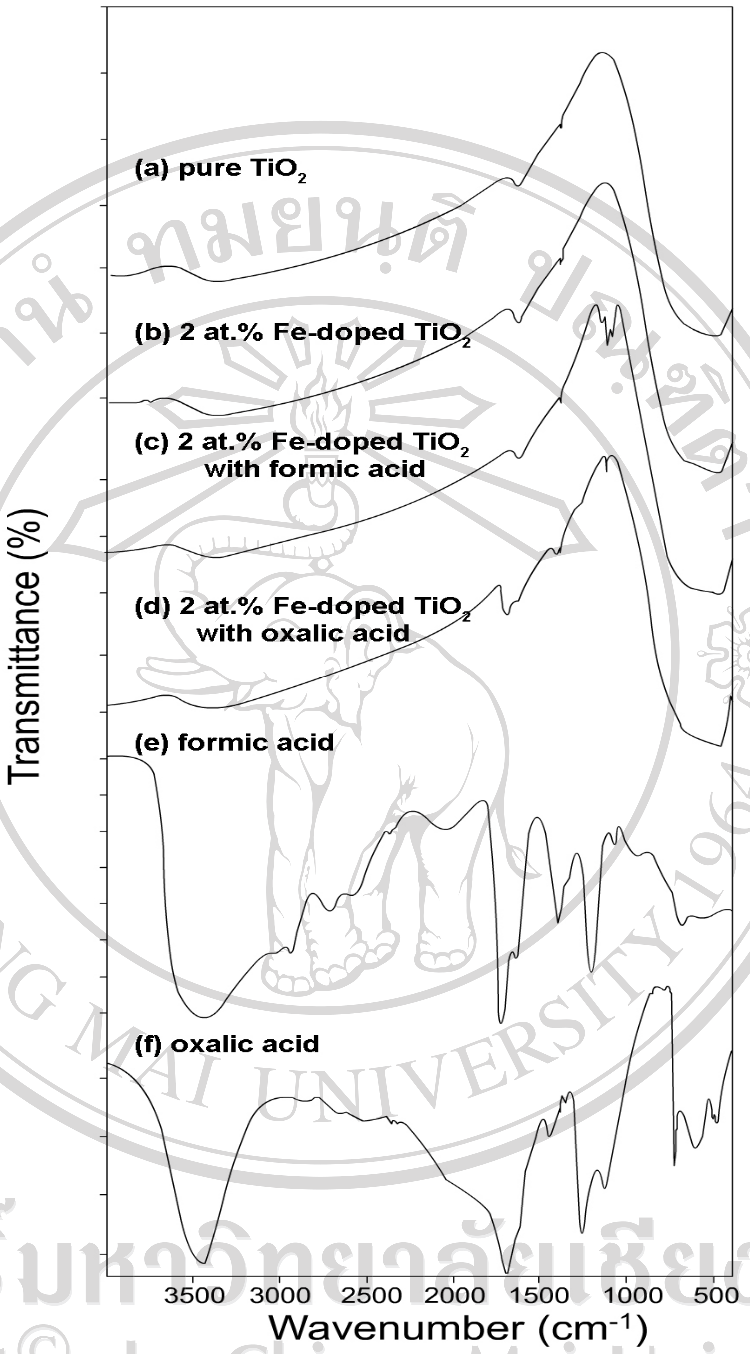

Figure 3.48 FT-IR spectra of (a) pure TiO_2, (b) 2 at.% of Fe-doped TiO_2 (the impregnation method, (c) 2 at.% of Fe-doped TiO_2 with formic acid, (d) 2 at.% of Fe-doped TiO_2 with oxalic acid after mineralization under visible light for 15 min, (e) formic acid, and (f) oxalic acid

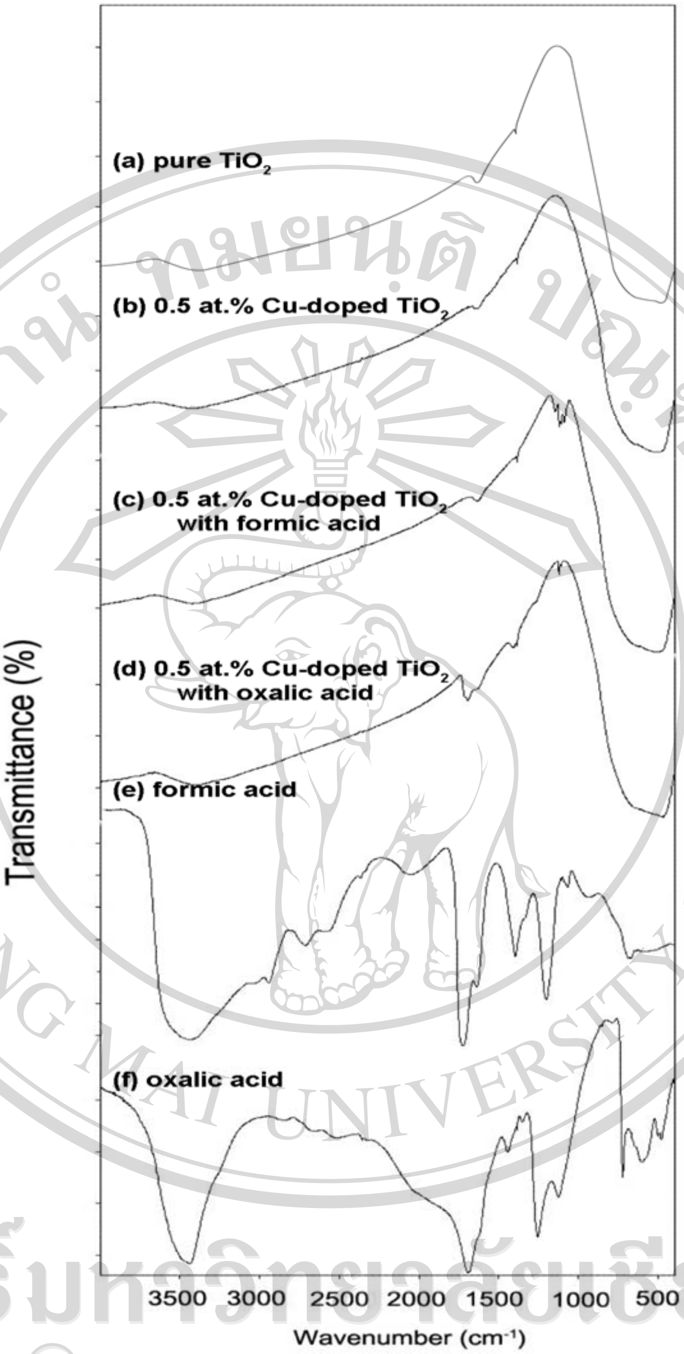

Figure 3.49 FT-IR spectra of (a) pure TiO_2, (b) 0.5 at.% of Cu-doped TiO_2, (c) 0.5 at.% of Cu-doped TiO_2 with formic acid, (d) 0.5 at.% of Cu-doped TiO_2 with oxalic acid after mineralization under visible light for 15 min, (e) formic acid, and (f) oxalic acid

The ability of Fe-oxalate complexes involved in photochemical oxidation reactions has already been mentioned in the literatures [119-120]. Ferrioxalate is one of the best known examples of Fe^{3+}-polycarboxylate complexes. Ferrioxalate could absorb over a broad range of wavelengths (UVA (340-400 nm) and visible region (400-700 nm)) and utilize more efficiently on visible radiation. A recent investigation by Teoh *et al.* [43] in Fe-doped TiO_2 prepared by Flame Spray Pyrolysis (FSP) proposed that Fe^{3+} formed a complex with oxalate which was easily photolyzed to produce CO_2 and Fe^{2+} ions under visible light irradiation. The photocatalytic activity of the FSP Fe-doped TiO_2 could be re-generated by the oxidation of adsorbed Fe^{2+} to Fe^{3+} under visible light irradiation.

The complex of Fe^{3+}-oxalate when photolyzed could exist either in the state of dissociation of oxalate radical ($C_2O_4^{\cdot -}$) from surface or transfer into solution was reported by Mazellier and Sulzberger [120]. The oxalate radical $(C_2O_4)^{\cdot -}$ reacted with oxygen molecule to produce $O_2^{\cdot -}$ and $HO_2^{\cdot}$ then $HO_2^{\cdot}$ was ended as H_2O_2 (reaction (3.10)-(3.15)), which subsequently form hydroxyl radical $OH^{\cdot}$. Hydrogen peroxide formed from $HO_2^{\cdot}/O_2^{\cdot -}$ was another significant oxidant for Fe^{2+} in aqueous solution production of hydroxyl radical (reaction(3.15)). Formation of H_2O_2 via photoexcitation of Fe^{2+} was also unlikely especially at acidic pH, hence ruling out the possibility of Fenton or photo-Fenton reactions. The rate constants of Fe^{2+} in aqueous, the oxidation by $HO_2^{\cdot}/O_2^{\cdot -}$ and by H_2O_2 depending critically on the Fe^{2+} in aqueous solution was presented as dissolved Fe^{3+}-oxalate complexes that underwent photolysis, leading ultimately to $OH^{\cdot}$ production [119]. Fe^{3+}-oxalate coexist could occur a photo-Fenton-like system and produced $OH^{\cdot}$ without external H_2O_2. Hydrogen peroxide is a direct source of hydroxyl radical in photo-Fenton system.

The high mineralization of oxalic acid using Fe-doped TiO_2 was postulated that this redox reaction of Fe^{3+}-oxalate complex under photolyzed could generate hydroxyl radical (Equation (3.9)-(3.14). Many researchers [119,123-124] described Fenton reaction as known to be a very effective way in the removal of organic pollutants for wastewater treatment. Hydroxyl radical ($OH^{\bullet}$) produced with high reactivity and degraded most of organic compounds.

$$[Fe^{3+}(C_2O_4)_3]^{3+} + h\nu \longrightarrow [Fe^{2+}(C_2O_4)_2]^{2-} + C_2O_4^{\bullet -} \qquad (3.9)$$

$$C_2O_4^{\bullet -} + [Fe^{3+}(C_2O_4)_3]^{3-} \longrightarrow [Fe^{2+}(C_2O_4)_2]^{2-} + C_2O_4^{2-} + 2CO_2 \qquad (3.10)$$

$$C_2O_4^{\bullet -} + O_2 \longrightarrow O_2^{\bullet -} + 2CO_2 \qquad (3.11)$$

$$2HO_2^{\bullet}/O_2^{\bullet -} \xrightarrow{H^+/2H^+} H_2O_2 + O_2 \qquad (3.12)$$

$$Fe^{2+} + 2HO_2^{\bullet}/O_2^{\bullet -} \xrightarrow{H^+/2H^+} Fe^{3+} + H_2O_2 \qquad (3.13)$$

$$Fe^{2+} + H_2O_2 \longrightarrow Fe^{3+} + HO^{\bullet} + OH^{-} \qquad (3.14)$$

The important factors as pH value and dopant concentration to form Fe^{3+}-oxalate complex in order to produce highly hydroxyl radical as Balmer et al. [121-122] reported that when the pH was around 4, the main Fe^{3+}-oxalate species were $Fe^{3+}(C_2O_4)_2^{-}$, $Fe^{3+}(C_2O_4)_3^{3-}$, which generated more $OH^{\bullet}$. Some researchers investigated photocatalytic activity of Fe-doped TiO_2 and found that it was strongly dependent on the dopant concentration [122]. Generally, not all metal ions can react through photo-Fenton reaction in the absence of H_2O_2, but the oxidation rate can be increased by addition of external hydrogen peroxide. In contrast, if the metal is deposited onto the semiconductor surface, Fenton-type reactions cannot take place. In addition, it was found that Fenton reactions can be improved by light then the former becoming photo-Fenton reactions. In the same way, Cu^{2+}-oxalate complex could be occurred in the redox reaction as the same as the Fe^{3+}-oxalate complex.

The formic acid could be degraded according to the following reactions (3.15)-(3.16).

$$Fe^{3+} + HCOOH \longrightarrow [HCO_2\text{-}Fe]^{2+} + H^+ \quad (3.15)$$

$$[HCO_2\text{-}Fe]^{2+} + O_2 \longrightarrow Fe^{2+} + HO_2^{\bullet} + CO_2 \quad (3.16)$$

Degradation in the solution with Fe^{2+} could take place through the reaction of the $OH^{\bullet}$ radicals formed during the oxidation of Fe^{2+} according to the reactions (3.17)-(3.20).

$$Fe^{2+} + O_2 \longrightarrow Fe^{3+} + O_2^{\bullet-} \quad (3.17)$$

$$O_2^{\bullet-} + H^+ \longrightarrow HO_2^{\bullet} \quad (3.18)$$

$$HO_2^{\bullet} + Fe^{2+} + H^+ \longrightarrow H_2O_2 + Fe^{3+} \quad (3.19)$$

$$Fe^{2+} + H_2O_2 \longrightarrow Fe^{3+} + OH^- + OH^{\bullet} \quad (3.20)$$

Also, the redox reactions of Cu^{2+}-oxalate could be the same as the redox reaction of Fe^{3+}-oxalate according to the reactions (3.21)-(3.24).

$$Cu^{2+} + HCOOH + H^+ \longrightarrow Cu^+ + CO_2 + 2H^+ \quad (3.21)$$

$$Cu^+ + \frac{1}{2}O_2 + e^- + 2H^+ \longrightarrow H_2O + Cu^{2+} \quad (3.22)$$

$$Cu^{+} + HO_2 + H^{+} \longrightarrow Cu^{2+} + H_2O_2 \qquad (3.23)$$

$$Cu^{+} + H_2O_2 \longrightarrow Cu^{2+} + OH^{\bullet} + OH^{-} \qquad (3.24)$$

Recently, Litter (1999) [125] observed that the effect of complexation was strongly depended on the type and concentration of the metal ion: both an increase in the photooxidation rate and a detrimental effect was observed. The optimal concentration enhanced the rate of the photocatalytic activity. The detrimental effect of high metal ion concentrations on the oxidation rate was explained by different factors. Firstly, high amounts of metallic species compete generally with oxygen by conduction band electrons, reducing the generation of $HO^{\square}$. Another reason for the deleterious effect of high concentrations of Fe^{2+}, Cu^{2+} or Ni^{2+} was found due to UV light absorption of the species. Finally, the decreasing in the rate could be caused by precipitation of dissolved metals as hydroxides onto the surface of the catalyst or by reflection of UV radiation.

In our study the enhancement of Fe-doped TiO_2 on the mineralization of oxalic acid and formic acid could be concluded from the formation of Fe^{3+}-oxalate and Fe^{3+}-formate complex. The interaction of between Fe^{3+}-oxalate and the possibility of Fe^{3+}-oxalate complexation were studied by using FT-IR analysis. The FT-IR peaks of 2 at.% Fe-doped TiO_2 with adsorbed oxalic acid at 1400 and 1200 cm^{-1} had higher intensity than those in bare TiO_2. The spectra of adsorbed oxalate ions obtained from this study indicated that oxalate ions form strong surface complexes on Fe-doped TiO_2 surface. Fe^{3+}-oxalate complex could be strongly absorbed at low pH. FT-IR results showed that Fe^{3+}-oxalate formed a complex. The enhanced performance observed for the Fe-doped TiO_2 system was likely due to the formation of ferrioxalate complex that could be generated hydroxyl radical.